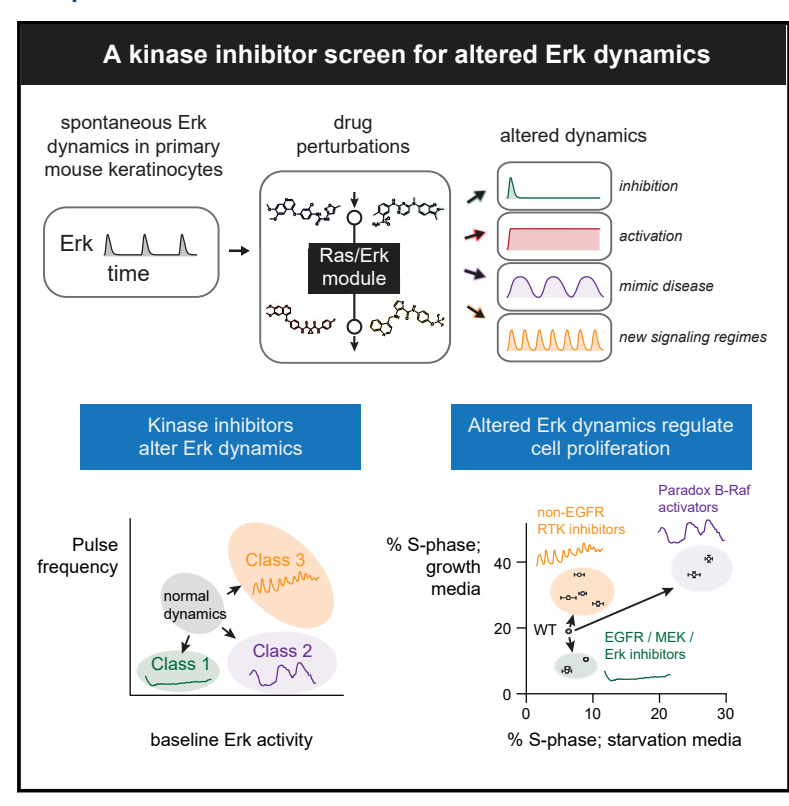
# **Cell Systems**

# A Live-Cell Screen for Altered Erk Dynamics Reveals Principles of Proliferative Control

## **Graphical Abstract**



### **Highlights**

- Keratinocytes exhibit robust, rapid Erk pulses even without exogenous growth factors
- Screening 429 kinase inhibitors reveals distinct perturbations to Erk dynamics
- Receptor tyrosine kinase inhibition can increase Erk activity and pulse frequency
- Optogenetic control reveals how Erk dynamics alter cell proliferation

### **Authors**

Alexander G. Goglia, Maxwell Z. Wilson, Siddhartha G. Jena, Jillian Silbert, Lena P. Basta, Danelle Devenport, Jared E. Toettcher

### Correspondence

toettcher@princeton.edu

### In Brief

Goglia et al. identified modulators of Erk dynamics by screening a library of 429 kinase inhibitors and monitoring Erk activity over 5 h in more than 80,000 single primary mouse keratinocytes. They identified both known and uncharacterized modulators, including inhibitors of non-EGFR receptor tyrosine kinases (RTKs) that increased Erk pulse frequency and overall activity. Their work opens the door to high-throughput screens using live-cell biosensors and reveals that cell proliferation integrates information from Erk dynamics as well as additional permissive cues.





Cell<sup>2</sup>ress



# A Live-Cell Screen for Altered Erk Dynamics Reveals Principles of Proliferative Control

Alexander G. Goglia, <sup>1,2</sup> Maxwell Z. Wilson, <sup>1,2</sup> Siddhartha G. Jena, <sup>1,3</sup> Jillian Silbert, <sup>1,3</sup> Lena P. Basta, <sup>1</sup> Danelle Devenport, <sup>1</sup> and Jared E. Toettcher <sup>1,4,\*</sup>

<sup>1</sup>Department of Molecular Biology, Princeton University, Princeton, NJ 08544

\*Correspondence: toettcher@princeton.edu https://doi.org/10.1016/j.cels.2020.02.005

### **SUMMARY**

Complex, time-varying responses have been observed widely in cell signaling, but how specific dynamics are generated or regulated is largely unknown. One major obstacle has been that highthroughput screens are typically incompatible with the live-cell assays used to monitor dynamics. Here, we address this challenge by screening a library of 429 kinase inhibitors and monitoring extracellular-regulated kinase (Erk) activity over 5 h in more than 80,000 single primary mouse keratinocytes. Our screen reveals both known and uncharacterized modulators of Erk dynamics, including inhibitors of non-epidermal growth factor receptor (EGFR) receptor tyrosine kinases (RTKs) that increase Erk pulse frequency and overall activity. Using drug treatment and direct optogenetic control, we demonstrate that drug-induced changes to Erk dynamics alter the conditions under which cells proliferate. Our work opens the door to high-throughput screens using live-cell biosensors and reveals that cell proliferation integrates information from Erk dynamics as well as additional permissive cues.

### INTRODUCTION

Animal cells must respond to a large number of external cues to function appropriately during development and adult tissue homeostasis. To that end, a typical mammalian cell is endowed with hundreds of distinct receptors, yet only a few signaling pathways downstream of these receptors are tasked with responding to these many inputs. For instance, the 58 human receptor tyrosine kinases (RTKs) activate on the order of ten intracellular pathways (e.g., Ras-Erk, PI3K-Akt, Src, PLCγ, and calcium) yet can trigger diverse downstream cellular responses in developing and adult tissues (Downward, 2001; Lemmon and Schlessinger, 2010). Cells are thus faced with the challenge of accurately transmitting information from many upstream inputs using only a few "wires" or signal transduction pathways.

One resolution to this paradox comes in the form of dynamic regulation. Two receptors may trigger different time-varying re-

sponses from a single pathway, which can then be interpreted into distinct fates (Marshall, 1995). Indeed, many core mammalian signaling pathways have now been observed to generate complex, time-varying signaling behaviors in response to certain input stimuli (Purvis and Lahav, 2013). A growing body of evidence suggests that these dynamics are relevant to normal cell function: extracellular-regulated kinase (Erk) and p53 pulses have been observed in vivo with similar timescales to those found in cultured cells (de la Cova et al., 2017; Hamstra et al., 2006; Hiratsuka et al., 2015) and disease-associated Ras-Erk pathway mutations can alter dynamics in a manner that affects cell proliferation (Bugaj et al., 2018). Yet it largely remains an open question how signaling dynamics are generated, regulated, and interpreted. We reasoned that a powerful tool to address this question would be to conduct a screen using signaling dynamics as a phenotypic readout (Behar et al., 2013; Stewart-Ornstein and Lahav, 2017).

Such a screen could potentially generate many useful insights. Perturbations to certain signaling nodes might eliminate dynamics altogether (Figure 1A, top), identifying essential components for producing time-varying responses. Others might switch dynamics between normal and diseased states (Figure 1A, middle), suggesting intervention points to correct aberrant signaling. Finally, some perturbations might result in hitherto-unobserved signaling dynamics (Figure 1A, bottom). These novel dynamic responses are analogous to classical mutant phenotypes, which can be highly informative despite (or because of) their differences from what is normally observed (Nüsslein-Volhard and Wieschaus, 1980).

Motivated by these possibilities, we set out to develop a screen for altered Erk signaling dynamics. Erk signaling is an ideal model system both because of its stimulus-dependent dynamics (Marshall, 1995) and the excellent tools available for monitoring and controlling pathway dynamics in individual cells (Regot et al., 2014; Toettcher et al., 2013). We also report an excellent experimental model system for screening Erk dynamics: primary mouse keratinocytes, which we found to exhibit rapid, robust, and reproducible Erk dynamics even in the absence of externally supplied growth factors. Screening a panel of 429 kinase inhibitors in more than 85,000 individual keratinocytes revealed multiple classes of altered Erk dynamics. The screen also uncovered previously uncharacterized regulatory links: inhibiting the non-epidermal growth factor receptor (EGFR) RTKs Met and vascular endothelial growth factor receptor (VEGFR) unexpectedly increased Erk's steady-state activity and pulse frequency. Using optogenetic stimuli to directly



<sup>&</sup>lt;sup>2</sup>These authors contributed equally

<sup>&</sup>lt;sup>3</sup>These authors contributed equally

<sup>&</sup>lt;sup>4</sup>Lead Contact

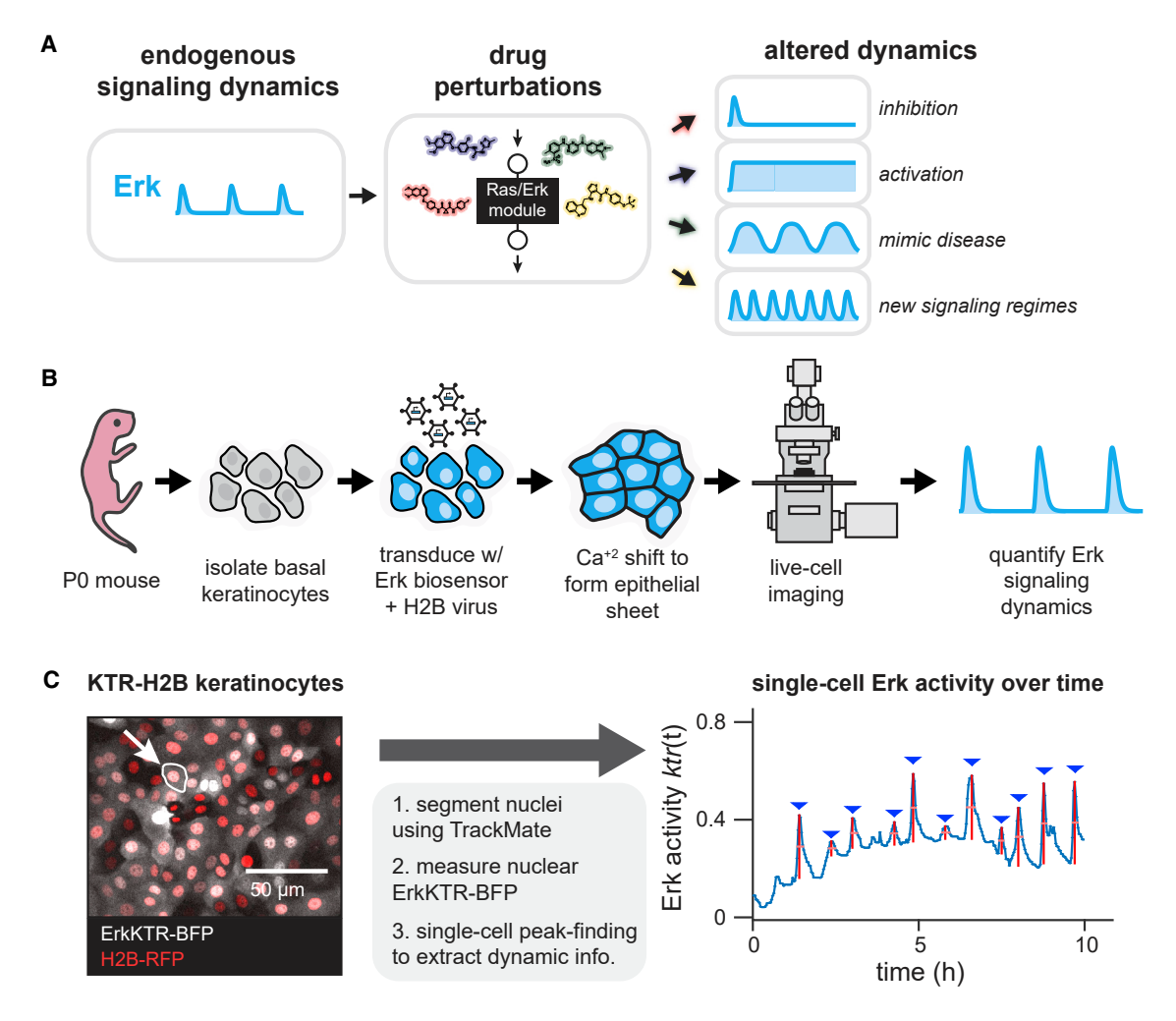


Figure 1. High-Throughput Screening for Altered Erk Dynamics

(A) A small-molecule screen for altered signaling dynamics. Such a screen can identify altered signaling behaviors including total pathway inhibition, constitutive activation, dynamics that resemble disease states, or previously undescribed dynamic regimes.

(B) Primary keratinocytes as a model system for quantitative studies of Erk signaling dynamics. Basal epidermal keratinocytes are isolated from a P0 mouse pup, transduced with viral vectors encoding live-cell biosensors, induced to form a uniform epithelial sheet, and imaged via confocal microscopy.

(C) An image processing pipeline for monitoring Erk dynamics. A fluorescent nuclear marker enables automated cell segmentation, tracking, and quantification of nuclear Erk KTR activity. A representative image of KTR-BFP- and H2B-RFP-expressing primary mouse keratinocytes is shown, as well as quantification of Erk activity from the indicated cell.

control Ras-Erk dynamics confirmed that these drug-induced changes to dynamics are sufficient to alter cell proliferation. Our work thus begins to define the molecular processes that govern and regulate dynamic Erk activity, provides a compendium of drug-induced changes to signaling dynamics, and establishes an extensible experimental and computational platform for future live-cell screens.

### **RESULTS**

### Primary Keratinocytes Are a Robust Model System for Pulsatile Erk Dynamics

We first needed to identify a cellular model of Erk dynamics that would be suitable for live-cell screening. Such a system must be highly dynamic, with frequent Erk pulses observed in a majority of cells. Dynamics should also be reproducible from day to day

and robust to variations in conditions (e.g., media formulations and time post-plating). It was recently reported that Erk is highly dynamic in the basal epithelium of live adult mice (Hiratsuka et al., 2015) and cultured epidermal keratinocytes (Waters et al., 2014), cells that can be cultured ex vivo without transformation or immortalization and are readily accessible to viral gene transduction and imaging (Nowak and Fuchs, 2009). We thus hypothesized that keratinocytes might serve as an ideal cell type to use as the basis for further dissection of Erk signaling dynamics.

We harvested basal keratinocytes from newborn CD1 mouse pups using established protocols (see STAR Methods) (Nowak and Fuchs, 2009). After 10 passages, we transduced primary keratinocytes with viral vectors encoding a blue fluorescent protein (BFP)-tagged biosensor of Erk kinase activity (kinase translocation reporter [BFP-KTR]) and a red fluorescent protein (RFP)-tagged histone H2B (H2B-RFP) (Figure 1B) (Regot

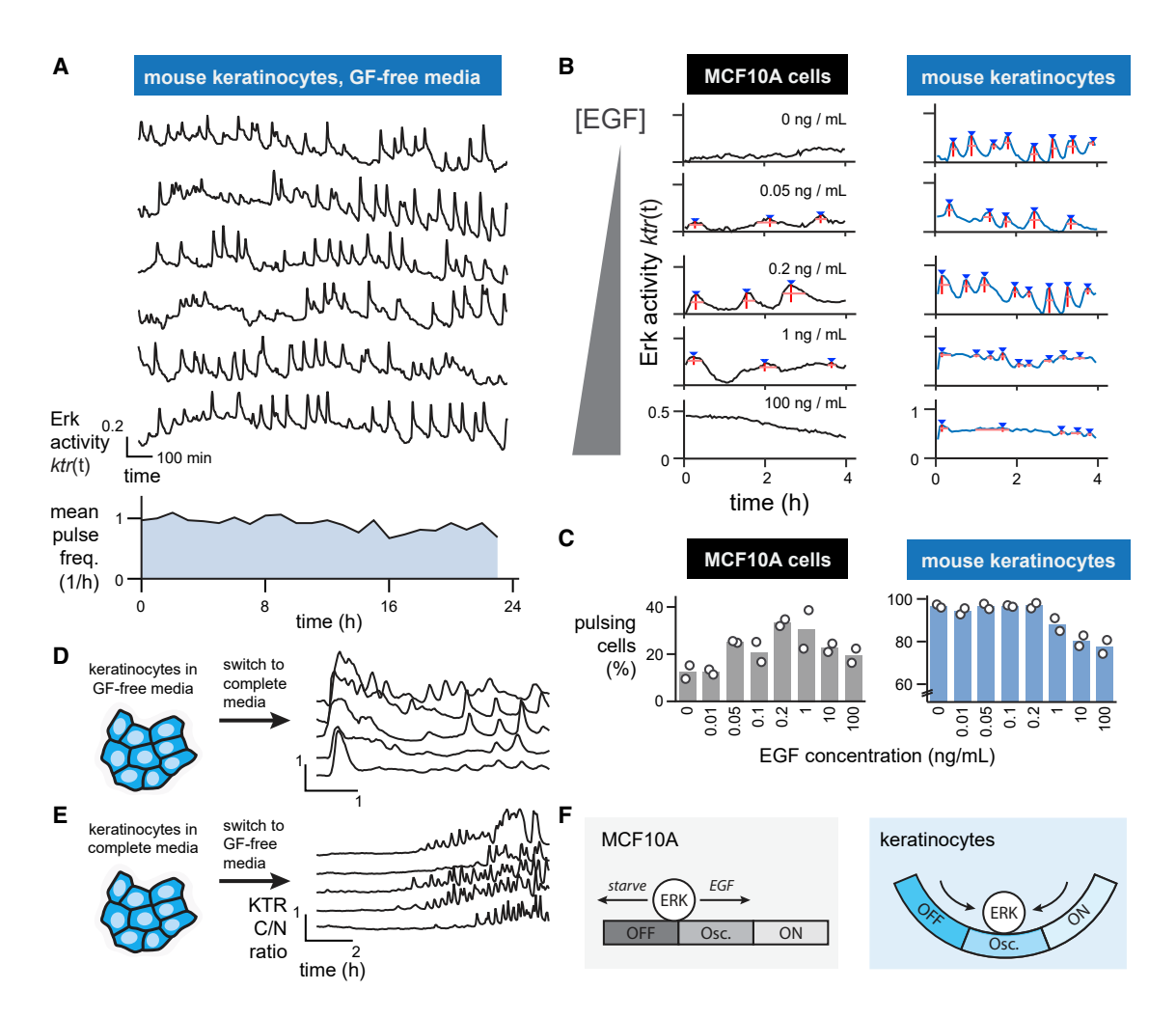


Figure 2. Primary Keratinocytes Exhibit an "Idling Motor" Ground State of Pulsatile Erk Dynamics

(A) Upper: representative single-cell traces of Erk activity in keratinocytes cultured in GF-free media over 24 h. Lower: the mean number of pulses observed per cell for each hour over the 24-h time course.

- (B) Representative single-cell traces for MCF10A breast epithelial cells (left) and mouse keratinocytes (right) treated with increasing doses of EGF.
- (C) The percentage of MCF10As (left) or mouse keratinocytes (right) that exhibited  $\geq 2$  Erk pulses over a 5-h time course after treatment with increasing doses of EGF. N = 2 biological replicates (white circles); each replicate includes data from >100 single cells.
- (D and E) Representative single-cell traces of Erk activity in keratinocytes shifted from GF-free media to complete media (in D) and from complete to GF-free media (in E) showing the reappearance of pulsatile Erk dynamics over time.
- (F) Schematic comparing the stimulus dependence of pulsatile Erk dynamics in classical cell lines, such as MCF10As (left) and primary keratinocytes (right). Instead of a flat landscape where dynamics are permanently altered by GF stimulation, keratinocytes adapt and return to a "ground state" of pulsatile Erk dynamics.

et al., 2014). We sorted these cells to obtain a homogenous population of dual-expressing, low-passage-number keratinocytes (termed KTR-H2B keratinocytes) that were used for all subsequent experiments. For analysis, we segmented and tracked H2B-RFP-positive nuclei, obtained nuclear KTR-BFP intensity for each cell, and quantified features of pulsatile Erk activity using the ImageJ plugin TrackMate and custom MATLAB code (Figures 1C and S1; STAR Methods) (Abràmoff et al., 2004; Jaqaman et al., 2008; Tinevez et al., 2017).

We first set out to characterize baseline Erk activity dynamics in primary mouse keratinocytes. KTR-H2B keratinocytes were plated on fibronectin-coated glass, switched to high-calcium conditions to form an epithelial monolayer and starved in growth factor-free (GF-free) media for 8 h prior to imaging. We observed

frequent pulses of Erk activity in most cells, even though these conditions lacked any externally supplied growth factors, serum, or other additives (Figure 2A, top; Video S1). Quantifying Erk dynamics revealed that they were relatively stable over 24 h of imaging, with cells pulsing approximately once per hour on average (Figure 2A, bottom). Analysis of the timing between successive pulses revealed a broad distribution of waiting times with a long tail, suggesting that keratinocytes may exhibit stochastic, excitable Erk activity pulses rather than regular, periodic oscillations (Figures \$2A and \$2B). Similar Erk activity pulses were observed across a range of culture conditions, including skin-like organotypic cultures at an air-liquid interface (Figures \$2C—\$2E) (Aw et al., 2016). Immunostaining in embryonic mouse epidermis also revealed a salt-and-pepper pattern of Erk phosphorylation

(Figure S2F), consistent with similar sporadic bouts of Erk activity in epidermal cells *in vivo* (Hiratsuka et al., 2015).

Unlike our observations in keratinocytes, prior studies in various epithelial cell lines found Erk dynamics to be strongly dependent on growth factors and culture conditions (Albeck et al., 2013; Aoki et al., 2013; Shankaran et al., 2009). We thus sought to directly compare keratinocytes to MCF10A epithelial cells, a classic model cell line for studying Erk dynamics (Albeck et al., 2013). We treated KTR-H2B-expressing MCF10As or keratinocytes with varying doses of epidermal growth factor (EGF) and monitored Erk activity for 4 h after stimulation (Figures 2B and S2G; Video S2). In MCF10As, Erk dynamics varied as a function of EGF concentration, from low, constant Erk activity in the absence of EGF to occasional pulses at intermediate EGF doses (50-200 pg/mL) and constant, high Erk activity in the presence of saturating EGF. Only 30% of MCF10A cells pulsed at least twice over 4 h of imaging, even at the most permissive EGF concentrations (Figure 2C, left). In contrast, keratinocytes exhibited robust, frequent Erk pulses across a broad range of EGF concentrations (from GF-free to 1 ng/mL EGF), with 80%-100% of cells pulsing in all conditions tested (Figure 2C, right).

Our data led us to suspect that pulsatile Erk activity represents a baseline signaling state to which keratinocyte cells return even after strong external perturbations. To test this model, we monitored Erk activity dynamics after acutely switching keratinocytes from GF-free to complete media or from complete to GF-free media (Figures 2D and 2E). Cells exhibited a high-amplitude peak of Erk activity in response to serum stimulation, followed by adaptation and a return to spontaneous pulsing over 2-3 h (Figure 2D). Conversely, switching to GF-free media drove Erk to a constant, low-activity state for  $\sim$ 6 h, after which cells spontaneously resumed pulsing (Figure 2E). Pulsing did not require active transcription or EGF-family ligand shedding (Joslin et al., 2010), as pulses persisted in cells treated with the transcriptional inhibitor actinomycin D or an inhibitor of a disintegrin and metalloproteinase (ADAM)-family extracellular proteases. TAPI-1 (Figure S3) (Aoki et al., 2017; Hiratsuka et al., 2015). Primary mouse keratinocytes thus appear to harbor an "idling motor" of pulsatile Erk signaling to which they return even after strong signaling perturbations (Figure 2F).

What might the function of these idling-motor Erk activity pulses be? One clue may lie in the ability of pulsatile, excitable systems to generate synchronous, high-amplitude responses to weak external stimuli, as has been suggested for cortical actin oscillations in Dictyostelium cells (Hoeller et al., 2016). Supporting this model, we observed that KTR-H2B keratinocytes exhibited a synchronous pulse of Erk activity when stimulated with 50 pg/mL EGF (Figure S2H), a dose 20 times lower than what is required to elevate cells' overall Erk activity (1 ng/mL; Figure S2I). It is possible that this robust dynamic state may be a unique property of epidermal stem cells, perhaps related to their continuous lifelong proliferation. Alternatively, the pulsatile state may be a universal property of mammalian epithelia in vivo but has been lost over time in tissue-culture cell lines. A better understanding of in vivo Erk signaling dynamics will be crucial for discriminating these possibilities (Hiratsuka et al., 2015). Regardless, we concluded that keratinocytes' ubiquitous and rapid Erk activity pulses make them an ideal model system to screen for compounds and pathways that regulate signaling dynamics.

### An Imaging-Based Drug Screen for Altered Erk Dynamics

We next set out to perform an imaging-based screen for compounds that alter Erk signaling dynamics. We selected a small-molecule library consisting of 429 kinase inhibitors (Selleck Chemicals). Such a library is likely to be enriched for modulators of Erk dynamics, as kinase activity is a primary currency of MAPK signaling and crosstalk (Mendoza et al., 2011). Moreover, many kinase inhibitors have been developed to directly target EGFR-MAPK signaling and can be assessed as positive controls. Finally, increasingly comprehensive data on kinase inhibitor specificity are becoming available (Anastassiadis et al., 2011; Karaman et al., 2008; Moret et al., 2019), making it possible to move quickly from an initial hit to a candidate kinase target and potential molecular mechanism.

We developed an experimental approach to plate, starve, and stimulate KTR-H2B keratinocytes in 50 wells of a 384-well plate per imaging session (Figure 3A; see STAR Methods). Precise volumes of each drug were delivered to a clean plate using an acoustic liquid handler, and drugs were then diluted to working concentrations in GF-free media and transferred to plates of keratinocytes to a 2.5- $\mu$ M final concentration. Each batch of 50 wells included multiple vehicle-only (DMSO) controls to monitor batch-to-batch variability in Erk dynamics. We then performed two-color confocal imaging on 200 cells per drug every 3 min over 5 h, resulting in a total of  $\sim\!80,000$  cells tracked and analyzed across all conditions.

We extracted three features of nuclear Erk dynamics for each cell—the mean pulse frequency f; the mean pulse prominence p; and the mean pulse width  $t_{on}$  (Figures 3A and S1). While it is convenient to denote the average number of pulses per cell per unit time as a single-cell "frequency," our use of the term should not be taken to imply that Erk dynamics form a periodic oscillation versus stochastic, intermittent pulses. We also measured the mean KTR cytosol-to-nuclear ratio at each time point to obtain the overall Erk activity offset, a, for each drug. Finally, we quantified the density of cells and their total displacement over the 5-h time courses to test for indirect relationships between Erk dynamics and cell-physiological parameters. A pairwise correlation analysis revealed that cell density was positively correlated with the Erk activity offset a across all drugs (Figures S4A and S4B). Because plating density is an operatorcontrolled variable that is unrelated to which drug was added, we used a density-corrected Erk activity offset acorr for all analyses of the screen (Figure S4C). To verify that each of these metrics converges within our 5 h imaging period, we analyzed sub-intervals of the 24-h keratinocyte videos described above (Figures 2A, S2D, and S2E). We found that mean measurements (e.g., mean frequency and pulse prominence) converged within 2 h, whereas variance measurements (e.g., distribution of frequencies between individual cells) required more than 10 h for robust estimation (see STAR Methods). We thus focused on mean measurements per condition for all subsequent analyses.

Clustering by dynamic features revealed that most compounds did not alter Erk activity compared to DMSO controls, but that some drugs elicited strong changes in Erk dynamics (Figure 3B). To distinguish between different types of drug-induced dynamics, we performed principal component analysis on the matrix of compounds and dynamic measurements. This analysis revealed that the first two principal components (PCs) explained 88% of the dataset's overall variance, with PC1 dominated by temporal features

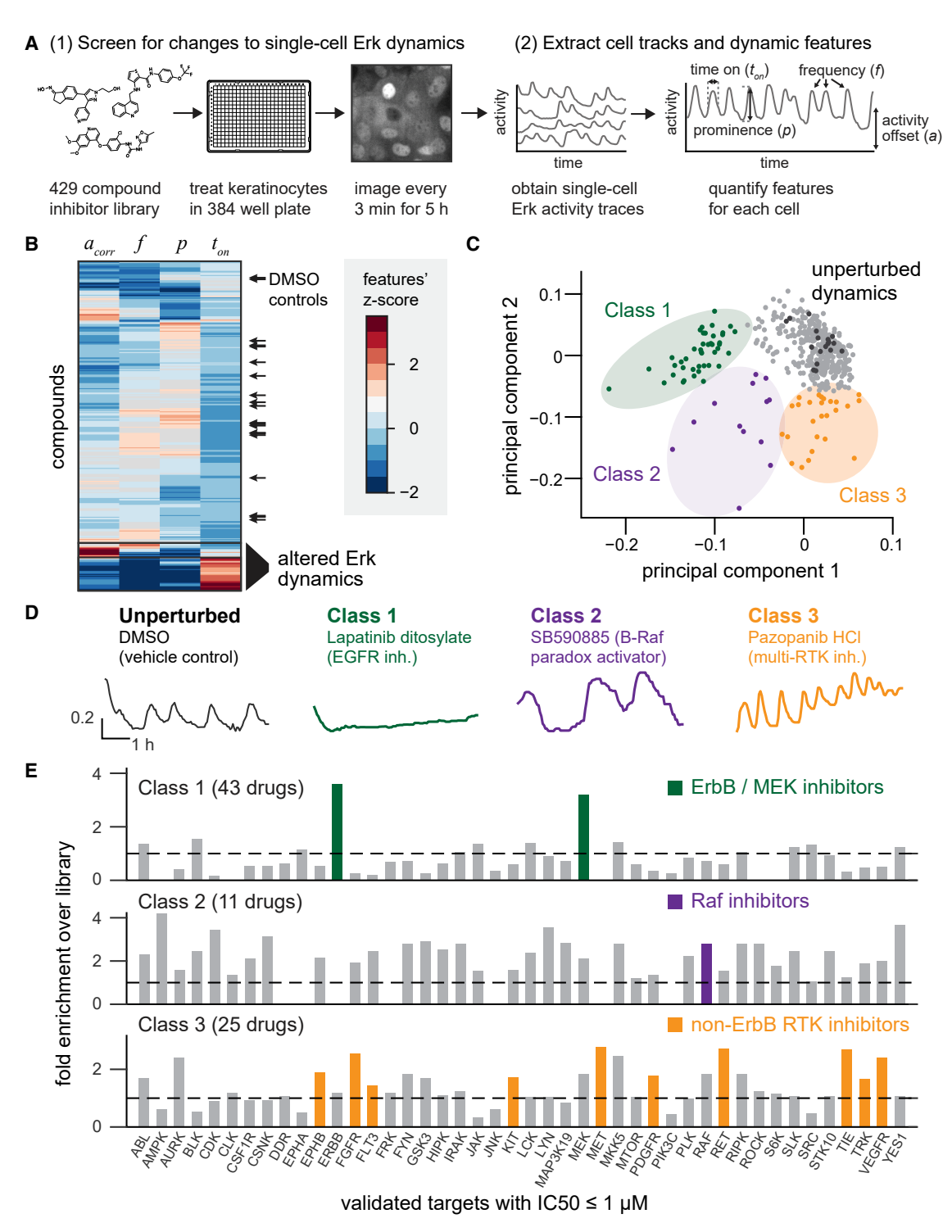


Figure 3. A Kinase Inhibitor Screen for Changes in Erk Dynamics

(A) Overview of experimental and computational steps in the small-molecule screen. KTR-H2B keratinocytes were plated in 384-well plates, treated with kinase inhibitors, and monitored every 3 min for 5 h H2B and KTR fluorescence images were used to track cells, assess Erk activity, and extract dynamic features for approximately 200 single cells per well.

- (B) Hierarchical clustering of all compounds by four dynamic features. Black arrows: DMSO controls from all 9 plates.
- (C) Principal component analysis showing the contribution of each compound along the first two PCs. Black dots indicate DMSO controls, and three classes of drug-induced perturbations are indicated.
- (D) Representative single-cell traces of Erk dynamics for one drug from each class. Drug name and the expected molecular target are indicated.
- (E) Enrichment analysis for drug targets in each class. Enrichment scores represent how many compounds hit a target within a class as compared to the overall compound library. Highlighted bars indicate enriched targets representing specific biological hypotheses for each class.

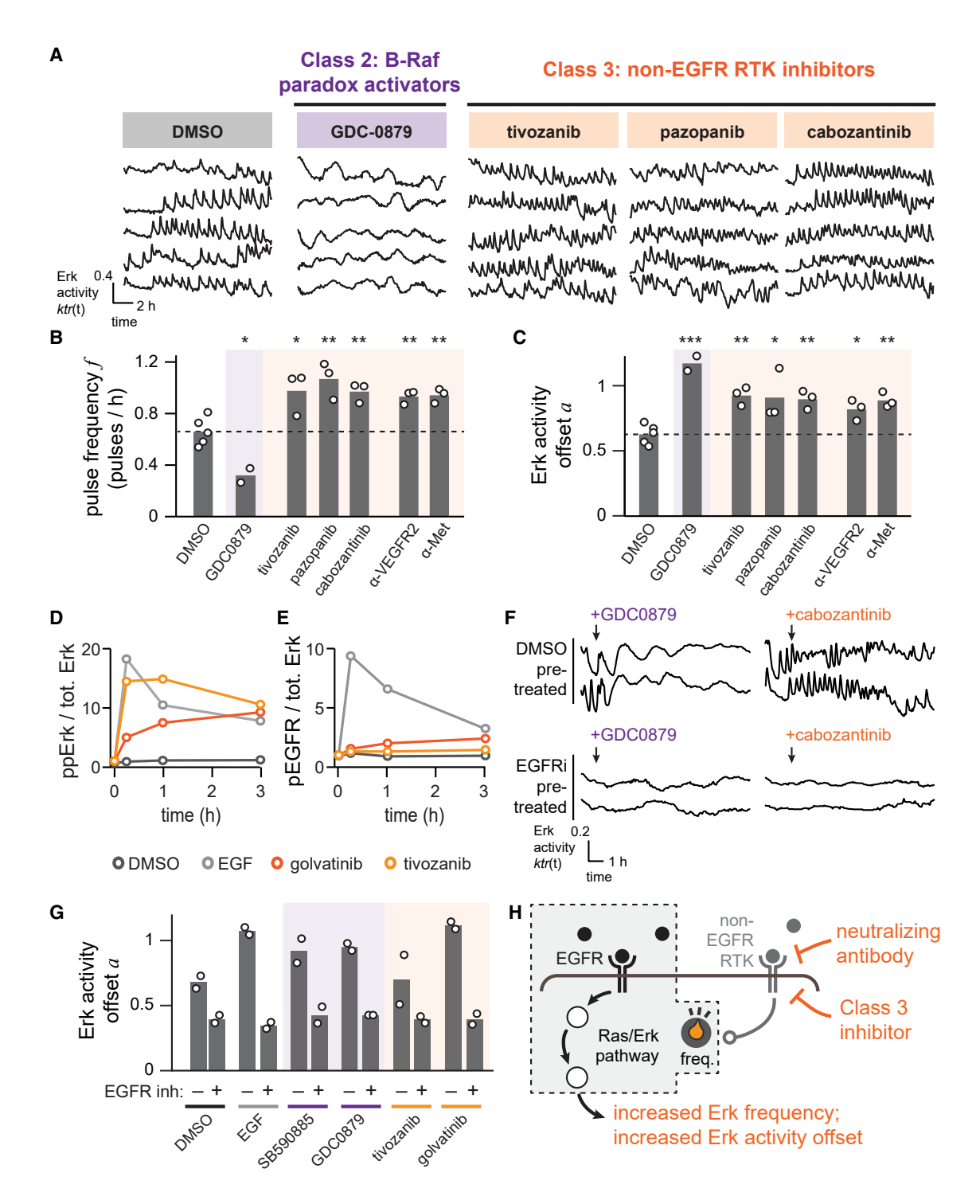


Figure 4. Inhibiting Non-EGFR Receptor Tyrosine Kinases Increases Dynamic Erk Activity in Keratinocytes

(A) Representative traces from keratinocytes treated with either a class 2 B-Raf inhibitor, a class 3 RTK inhibitor, or DMSO as a control. Cells were imaged every 3 min over 12 h.

(B and C) Average Erk pulse frequencies (in B) and overall Erk activity offset (in C) for keratinocytes treated as (in A) or with a neutralizing antibody targeting Met or VEGFR2. Each biological replicate (white circle) represents dynamics assessed from at least 100 single cells. Statistics are derived using a two-sided t test (\*p<0.05, \*\*p < 0.01, \*\*\*p < 0.001).

(D and E) Western blot quantification for phospho-Erk (ppErk; in D) and phospho-EGFR (pEGFR; in E) in keratinocytes after the addition of either EGF or a non-EGFR RTK inhibitor (golvatinib or tivozanib). pEGFR and ppErk are normalized to total Erk protein and each value is represented as fold-induction relative to the untreated initial time point.

of the Erk pulses (pulse frequency f and pulse width  $t_{on}$ ), and PC2 was dominated by the amplitude features (activity offset a and pulse prominence p) (Figure S4F). Mapping each drug onto these PCs revealed three classes of drugs that were well separated from the majority of compounds and DMSO controls (Figure 3C; Table S1). Supporting the association of PC1 and PC2 with Erk levels and timing, we found that plotting each compound's activity offset and pulse frequency was also able to cleanly separate all three drug classes (Figure S4G). Because of the noise inherent in a complex screen, we attempted to identify compounds and targets that were enriched within each class, rather than focusing undue attention on any single compound.

The first class of 43 Erk-altering inhibitors (referred to here as "class 1") (see Table S1) consisted of drugs that reduced Erk activity to a low, constant level, suggesting that this class may represent the canonical inhibitors of EGFR-MAPK signaling activity (Figure 3D; Video S3). A second class of 11 drugs (referred to here as "class 2") elevated Erk activity and decreased pulse frequency (Figure 3D; Video S3). Finally, a third class of 25 compounds (termed "class 3") amplified Erk activity by increasing the frequency and/or set point of Erk pulses (Figure 3D; Video S3).

To gain insight into the kinases targeted by each drug class, we compiled available information about each drug's molecular targets from Selleck Chemicals and the HMS LINCS project, a recently developed database of experimentally validated target information (Keenan et al., 2018; Moret et al., 2019). We then measured the enrichment of drug targets within each class over the entire library (Figure 3E; Supplemental Information). This analysis was immediately useful in the case of class 1 inhibitors, which was highly enriched for drugs with activity against EGFR-family (ErbB) receptors and the Erk-activating kinase MEK (Figure 3E; Table S1). Moreover, even class 1 drugs that were not annotated as EGFR-MEK inhibitors (e.g., saracatinib, TWS119, and ZM306416) have been implicated as direct inhibitors of these nodes in prior studies (Anastassiadis et al., 2011; Antczak et al., 2012; Formisano et al., 2015). Our drug screen thus correctly identified EGFR-MAPK pathway inhibitors as suppressors of dynamic Erk activity in keratinocytes. The observation that no other targets were enriched in this class also suggests that keratinocytes' pulsatile Erk dynamics do not require permissive activity from other canonical kinase signaling pathways.

The limited number of class 2 compounds precluded similarly informative enrichment analysis, as many kinases were only hit zero or one time (Figure 3E). However, examining individual drug responses revealed that two compounds in particular (SB590885 and GDC0879) elicited pronounced long, low-frequency Erk pulses (Figure 3D). Both compounds share a common classification as "paradox-activating" B-Raf inhibitors that increase Raf activity by stabilizing Raf-Raf dimers (Hall-Jackson et al., 1999; Hatzivassiliou et al., 2010; Heidorn et al., 2010; Poulikakos et al., 2010). These results are consistent with recent studies reporting that Erk dynamics are slowed in response to certain B-Raf P-loop mutations or treatment with paradox-activating B-Raf inhibitors in other

cellular contexts (Aoki et al., 2013; Bugaj et al., 2018). It is also notable that other paradox-activating B-Raf inhibitors in the compound library (e.g., vemurafenib) were not class 2 hits. This may be explained by the observation that SB590885 is an especially potent inducer of Raf dimerization at micromolar concentrations, unlike other paradox-activating inhibitors including vemurafenib (Miyamoto and Sawa, 2019). There may thus be a spectrum of paradoxical Raf activation, with changes in Erk dynamics reflecting the degree to which Raf dimers are stabilized.

We finally turned our attention to class 3 drugs, which elicited high-frequency Erk pulses on an elevated baseline (Figure 3D). Enrichment analysis revealed that no single kinase target was highly enriched; instead, we observed a broad enrichment for compounds that target many RTKs other than EGFR, including VEGFR, Met, Kit, and fibroblast growth factor receptor (FGFR) (Figure 3E). Conversely, class 1 was depleted for inhibitors targeting these same non-EGFR RTKs (Figure 3E). Importantly, the observation that EGFR inhibitors and non-EGFR RTK inhibitors have opposing effects on Erk activity in keratinocytes led us to hypothesize that various RTKs may exert antagonistic, inhibitory crosstalk on EGFR-driven Erk pulses. Such RTK-level crosstalk may provide a previously unappreciated layer of regulation over Erk dynamics, and we sought to better delineate its role in the following sections.

Our assessment of Erk dynamics relies on translocation of the fluorescent ErkKTR biosensor in and out of the nucleus, raising the possibility that differences we observe in ErkKTR dynamics may actually reflect drug-induced changes in overall nucleocytosolic transport rates. To control for this effect, we constructed a cell line expressing an optogenetic biosensor (irFP-LEXY) whose nucleocytosolic transport could be reversibly controlled by light and monitored in individual live cells (see STAR Methods) (Niopek et al., 2016). Monitoring the LEXY-based optogenetic biosensor's translocation in response to class 2 and class 3 hits revealed no changes in nuclear import-export kinetics (Figures S4H–S4I), further indicating that these compounds are bona fide regulators of Erk dynamics.

# Inhibiting Non-EGFR RTKs Tunes EGFR-Triggered Erk Dynamics

Our drug screen suggested that inhibitors of various RTKs might unexpectedly activate Erk, and we next sought to validate this class of targets and confirm their dynamics-altering effects. We focused on Met and VEGFR, RTKs whose inhibitors were especially potent for increasing Erk pulse frequency, and which have each been shown to be expressed in keratinocytes (Chmielowiec et al., 2007; Man et al., 2006; Wilgus et al., 2005) and to play functional roles in epidermal tissue proliferation, migration, or wound healing (Busch et al., 2008; Locatelli and Lange, 2011; Man et al., 2008; Wu et al., 2014). We repeated drug stimulus experiments with fresh aliquots of tivozanib (targeting VEGFR), pazopanib (VEGFR), cabozantinib (Met + VEGFR), and the class 2 compound GDC0879 (B-Raf), confirming that each drug was sufficient to alter Erk dynamics (Figure 4A; Video S4).

<sup>(</sup>F) Representative single-cell traces showing Erk activity in keratinocytes that were pre-treated for 1 h with the EGFR inhibitor lapatinib or DMSO control and then stimulated with EGF, class 2 or 3 inhibitors, or additional DMSO.

<sup>(</sup>G) The overall Erk activity offset a for cells treated as (in F). Each biological replicate (white circle) represents the mean of at least 100 cells imaged for 8 h. (H) A conceptual model of these results whereby inhibition of non-EGFR RTK by small molecules or neutralizing antibodies acts downstream of EGFR to enhance EGFR-driven pulsatile Erk signaling.

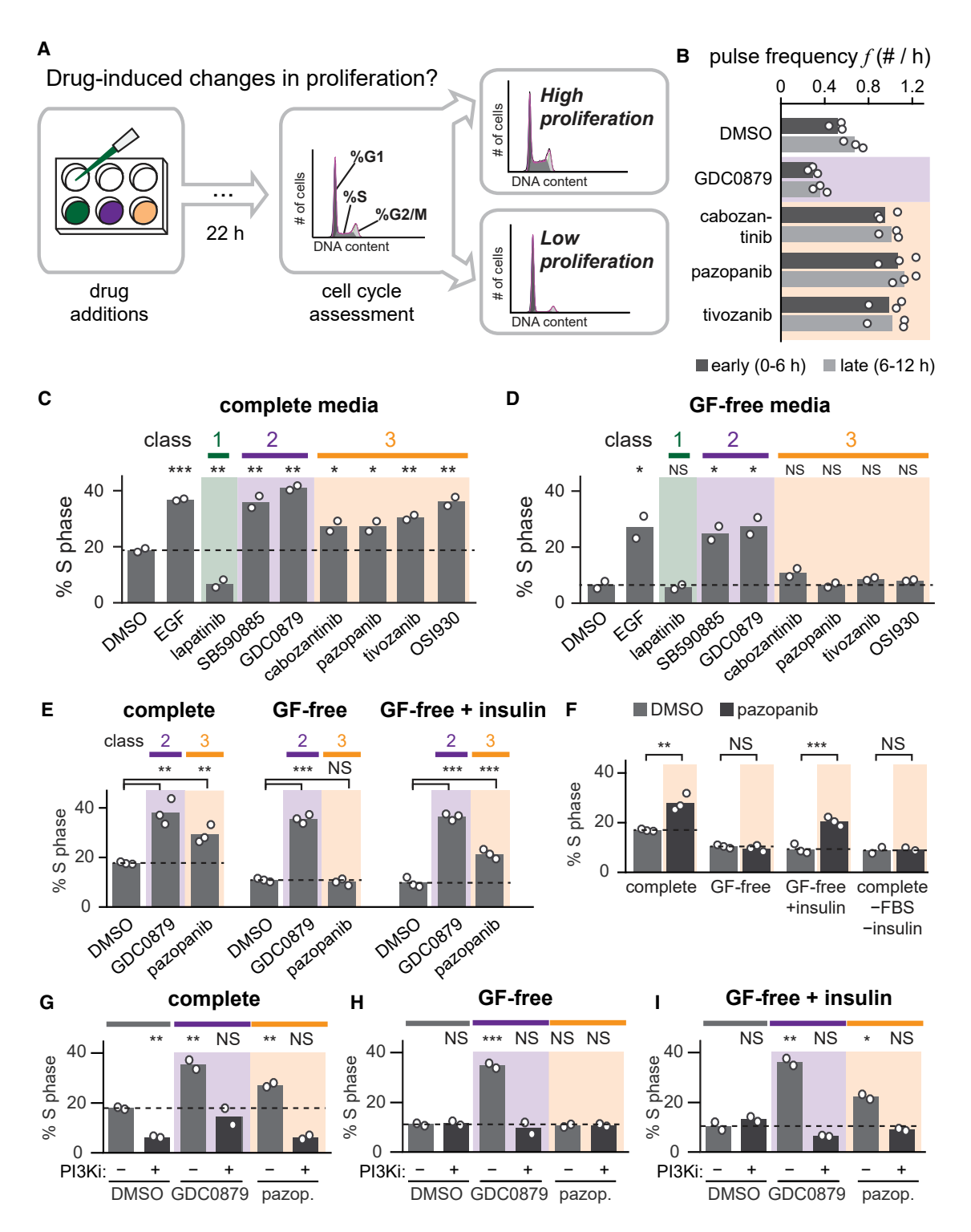


Figure 5. Drugs that Alter Erk Dynamics Have Distinct Effects on Cell Proliferation

(A) Schematic describing assay for cell proliferation in response to drug treatment. Keratinocytes are incubated for 22 h in the presence of a candidate compound and the resulting cell-cycle distribution is assessed by flow cytometry. The fraction of S phase cells is taken as a proxy for proliferation. For (C-I), biological replicates (white circles) were assessed from flow cytometry DNA content distributions of at least 20,000 cells each. Statistics are derived using a one-sided t test (\*p < 0.05, \*\*p < 0.01, \*\*\*p < 0.001).

(B) Quantification of Erk activity pulse frequency during the first and second halves of 14-h time courses after stimulation with class 2 and 3 compounds. Each biological replicate (white circle) represents the mean of least 100 single-cell trajectories.

(C and D) Quantification of cell proliferation (as described in A) for keratinocytes treated with compounds from class 1 (green), class 2 (purple), or class 3 (orange), EGF, or DMSO control and cultured in complete media (in C) or GF-free media (in D).

We next sought to confirm that Met and VEGFR are indeed the relevant molecular targets responsible for the change in Erk dynamics. We thus tested whether a separate class of inhibitors, neutralizing antibodies against RTKs' ligand-binding domains, could elicit similar responses. We treated KTR-H2B keratinocytes with either Met or VEGFR neutralizing antibodies, kinase inhibitors, or vehicle controls and monitored Erk dynamics over time. Class 3 kinase inhibitors and neutralizing antibodies targeting VEGFR and Met each elicited significant changes in Erk frequency and activity offset (Figures 4B and 4C). Together, these results demonstrate that inhibiting non-EGFR RTK activity indeed modulates Erk dynamics, raising the possibility that a broad range of clinical RTK inhibitors may unexpectedly act to increase EGFR-MAPK pathway activity in the skin.

How might inhibition of non-EGFR RTKs alter activity within the EGFR-Ras-Erk network? One possible nexus of crosstalk is the EGF receptor itself, as prior studies of cancer therapeutics indicate that inhibiting one family of RTKs can induce the expression and activation of parallel ligand-receptor pairs (Brand et al., 2014; Engelman et al., 2007). To test whether Met and VEGFR inhibition causes a corresponding increase in EGFR activity, we used immunoblotting to measure EGFR and Erk phosphorylation at various time points after addition of the VEGFR inhibitor tivozanib or the Met/VEGFR inhibitor golvatinib (Figures 4D, 4E, and S5). We observed high levels of Erk phosphorylation in response to both drugs, matching the increase in baseline Erk activity observed for class 3 compounds in the drug screen (Figure 4D). In contrast, EGFR phosphorylation was minimally affected by these compounds (Figure 4E). However, prior reports suggest that there is a high degree of amplification between EGFR and Erk (Krall et al., 2011; Pinilla-Macua et al., 2017), such that even a small increase in EGFR phosphorylation may still drive potent Erk activation. To account for this possibility, we measured the dose-response relationship between EGFR and Erk phosphorylation after 15 min of stimulation with various concentrations of EGF (Figure S5B). We found that even at the lowest EGF doses capable of driving high levels of Erk phosphorylation (1 ng/mL), EGFR phosphorylation was increased by approximately 3-fold (Figure S5C), much higher than that observed in the case of class 3 compounds at 15 min (less than 2-fold; Figures 4D and 4E). The positive effect of class 3 drugs on Erk activity cannot be explained solely by an increase in EGFR phosphorylation.

Our observations so far are consistent with two models. First, a compound might act to increase MAPK activity directly, functioning independently of EGFR-mediated activation. Alternatively, a compound may still require upstream receptor-level activity but increase the efficiency with which it is transmitted to the downstream MAPK network. This "gain-enhancement" model would be expected in the case of class 2 drugs, as it is known that paradox-activating Raf inhibitors still depend on upstream Ras activity for enhanced signaling (Heidorn et al., 2010). To distinguish between these possibilities, we monitored Erk dynamics after addition of both a class 2 or 3 compound and the

EGFR inhibitor lapatinib to block upstream receptor activity (Figures 4F and 4G). We found that in all cases, EGFR inhibitor pretreatment blocked the Erk-stimulatory effect of class 2 and 3 drugs. Taken together, our data support a model where inhibition of non-EGFR RTKs alters transmission through the intact EGFR-MAPK signaling pathway, tuning Erk's pulse frequency and overall activity level (Figure 4H).

# **Drug-Induced Changes to Erk Signaling Dynamics Have Distinct Effects on Cell Proliferation**

A growing body of literature suggests that signaling dynamics can be interpreted into specific cell fate outcomes (Johnson and Toettcher, 2019; Marshall, 1995; Purvis and Lahav, 2013). Yet in most cases, which dynamic features are sensed by cells to trigger a response is still unknown. We thus wondered whether the Erk dynamics observed in our pharmacological screen might also produce distinct cellular responses. In addition to revealing principles of cell fate control, such differences may be relevant to clinical responses after RTK inhibitor treatment. We focused on cell proliferation as a model Erk-driven cellular response (Figure 5A), as prior work has demonstrated that Erk activity is sufficient for proliferation under a range of conditions (Albeck et al., 2013; Aoki et al., 2013; Bugaj et al., 2018; Toettcher et al., 2013).

Mammalian cells' commitment to proliferation is thought to occur over an 8–12 h window, culminating in the onset of S phase (Zetterberg and Larsson, 1985; Zwang et al., 2011). We thus first set out to validate that drug-induced changes to Erk dynamics were persistent over at least the 8–12 h required for cell cycle entry. Using previously collected 14 h imaging data of Erk dynamics in response to compounds from each class (Figure 4A), we quantified dynamics separately in the first and second halves of the dataset. We observed similar drug-induced shifts to pulse frequency in both the first and second 7-h period (Figure 5B), indicating that drug-induced changes to dynamics are indeed sufficiently persistent to impact proliferation.

We next set out to assess drug-induced changes in cell proliferation. We first cultured keratinocytes in complete media, a condition that is permissive for proliferation but where drug-induced changes in Erk dynamics can still be observed (Figure S5). We then applied compounds from each of the three drug classes and measured the percentage of S phase cells after 22 h (Figure 5A). We found that the class 1 inhibitor lapatinib strongly reduced proliferation, consistent with a requirement for Erk activity to drive cell proliferation (Figures 5C and S7A). In contrast, class 2 and 3 compounds that increased overall Erk activity also enhanced proliferation, increasing the proportion of S phase cells comparable to a saturating dose of EGF.

Repeating the same experiment in GF-free media revealed similar responses in two cases: class 1 compounds suppressed proliferation, whereas class 2 compounds increased it. However, although class 3 compounds elicited high levels of proliferation in complete media, they were unable to drive cell proliferation in GF-free media (Figures 5D and S7B), even though they produce fast, frequent Erk pulses in both cases. These data raised the

<sup>(</sup>E) Quantification of cell proliferation (as described in A) for keratinocytes treated with GDC0879, pazopanib, or DMSO control and cultured in the indicated media. (F) Quantification of cell proliferation (as described in A) for keratinocytes treated with pazopanib or vehicle control in the indicated media.

<sup>(</sup>G-I) Quantification of cell proliferation (as described in A) for keratinocytes treated with GDC0879, pazopanib, or DMSO control in the presence or absence of the PI 3-kinase inhibitor pictilisib and cultured in complete media (for G), GF-free media (for H), or GF-free + insulin media (for I).

possibility that the not all Erk-activating stimuli are interpreted equally, and that the fast dynamics elicited by class 3 drugs may trigger proliferation under a more restrictive set of conditions than the slow dynamics elicited by class 2 drugs.

### Pazopanib Treatment and IGF1R-Insulin Receptor Signaling Cooperate to Drive Cell Proliferation

Our data so far suggest that class 3 drugs only increase cell proliferation in certain culture conditions, but serum contains a host of factors that may influence cell proliferation, thus obscuring any underlying mechanism. We thus set out to define the specific factors required for Class 3 drugs to elicit cell proliferation, using media formulations in which GF-free media was supplemented with defined growth media additives (Table S2). We monitored cell proliferation after treatment with pazopanib (a class 3 compound), GDC0879 (a class 2 compound), or vehicle control (Figures 5E and 5F). We found that a single additive, insulin, was sufficient for pazopanib treatment to trigger cell proliferation, increasing the fraction of S phase cells to the level observed in complete media (Figure 5F). Conversely, cells cultured in complete media lacking insulin and serum, but containing all other additives, failed to proliferate in response to pazopanib treatment (Figure 5F). In contrast, insulin had no effect on cell proliferation for cells treated with GDC0879 (which drove high proliferation with our without insulin) or vehicle control (which failed to induce proliferation regardless of insulin treatment) (Figure 5E). We also verified that insulin treatment does not itself trigger changes to Erk dynamics (Figures S7C-S7E). Taken together, these data demonstrate that a class 3 drug, pazopanib, acts in concert with IGF1-insulin receptor signaling to drive cell proliferation, whereas either stimulus alone is non-proliferative.

Prior studies suggest that some cell decisions may depend on combinations of Erk and Akt signaling, rather than either stimulus alone (Chen et al., 2012; Mendoza et al., 2011). As Akt is a primary effector of IGF1-insulin receptor signaling, we hypothesized that cell proliferation in response to high-frequency Erk pulses might also depend on insulin-induced PI3K-Akt signaling. To test this hypothesis, we first repeated the proliferation assays in the presence or absence of the PI3K inhibitor pictilisib (Figures 5G-5I). We found that pictilisib treatment suppressed proliferation in all media conditions and in response to all drugs, suggesting that PI3K-Akt activity is universally required for proliferation in our assays. We further reasoned that even if this pathway is absolutely required for proliferation, the specific level of PI3K-Akt signaling might tune the fraction of proliferating cells. However, measuring phospho-Akt levels revealed no clear relationship between PI3K-Akt pathway activity and proliferation when comparing class 2 versus class 3 drugs or complete versus GF-free media conditions (Figure S7F). Thus, while our data suggest high-frequency Erk dynamics co-require an additional cue from IGF1-insulin receptor signaling to trigger increased cell proliferation, the molecular pathways that achieve this integration remain to be defined.

# Optogenetic Stimuli Causally Link Erk Dynamics to Cell Proliferation

So far, we have seen that certain classes of kinase inhibitors alter both Erk dynamics and cell proliferation, but this correlative relationship must be interpreted with caution. Each drug may alter multiple features of Erk dynamics (e.g., pulse frequency and overall Erk activity) and likely acts on multiple kinase targets in the cell (Giuliano et al., 2018), making it impossible to unambiguously assign a dynamic response to a specific cellular outcome. We thus set out to directly control Erk dynamics and assess their effects on cell proliferation using an optogenetic strategy (Bugaj et al., 2018). We transduced keratinocytes with a blue-light-sensitive variant of the OptoSOS optogenetic system (Toettcher et al., 2013) that we have found to function robustly in contexts ranging from mammalian cells to *Drosophila* embryos (Guntas et al., 2015; Johnson et al., 2017).

Our goal is to completely control Erk dynamics with light, yet keratinocytes exhibit endogenous Erk pulses that could play a confounding role. We reasoned that pre-treatment with the class 1 drug lapatinib could be used to block endogenous EGFRinduced pulses, while still enabling us to deliver light inputs to Ras and activate Erk signaling on demand (Figure 6A). If successful, such a system would enable us to vary the frequency of light pulses to mimic the shifts in Erk dynamics that are elicited by class 2 and 3 drugs (Figure 6B). To validate this strategy, we monitored Erk dynamics in KTR-H2B-OptoSOS keratinocytes that were treated with lapatinib and toggled between darkness and blue light every 15 min. We observed consistent, controllable Erk dynamics for more than 8 h (Figure 6C; Video S5). Light stimuli can thus be used to precisely control Erk signaling even in cells that normally harbor complex, autonomous EGFR-driven signaling dynamics.

We next set out to measure proliferation in response to Erk activity dynamics that mimic the effects of class 2 and class 3 drugs. A primary difference between these two drug classes is their shift in the frequency of Erk pulses. To isolate the role of this frequency shift, we designed light inputs that maintained the same overall dose of blue light but were subdivided into pulses at different frequencies (10' on/10' off, 30' on/30' off, or 60' on/60' off). Pulses were delivered using an Arduino-microcontroller-driving light-emitting diode (LED) panels in a tissueculture incubator, and DNA content was again assessed after 22 h (see STAR Methods). We found that the proliferative responses triggered by optogenetic Ras/Erk pulses broadly matched those obtained previously from class 1, 2, and 3 compounds: both high-frequency and low-frequency light pulses partially restored proliferation in lapatinib-treated cells cultured in complete media (Figures 6D and S8A), just as had been observed for class 2 and class 3 inhibitors (Figure 5C). Optogenetic stimulation was also able to replicate the context dependence of high-frequency Erk pulses, which failed to induce proliferation in GF-free media (Figures 6D and S8B), just as had been observed for class 3 drugs (Figure 5D). Finally, 60' on/60' off pulses, reminiscent of the dynamics induced by paradox-activating Raf compounds, increased the proliferation of lapatinibtreated cells in both complete and GF-free media (Figure 6D).

Our optogenetic stimulation data cannot be explained by a simple model where proliferation is proportional to the total Erk dose (Gillies et al., 2017), as all of our pulsed-light stimuli contained the same overall light dose, yet elicited responses ranging from no proliferation (15' on/15' off) to maximal proliferation (60' on/60' off). Furthermore, we observed no differences in proliferation between cells that had been stimulated with either 60' on/60' off light pulses or continuous blue light, stimuli with

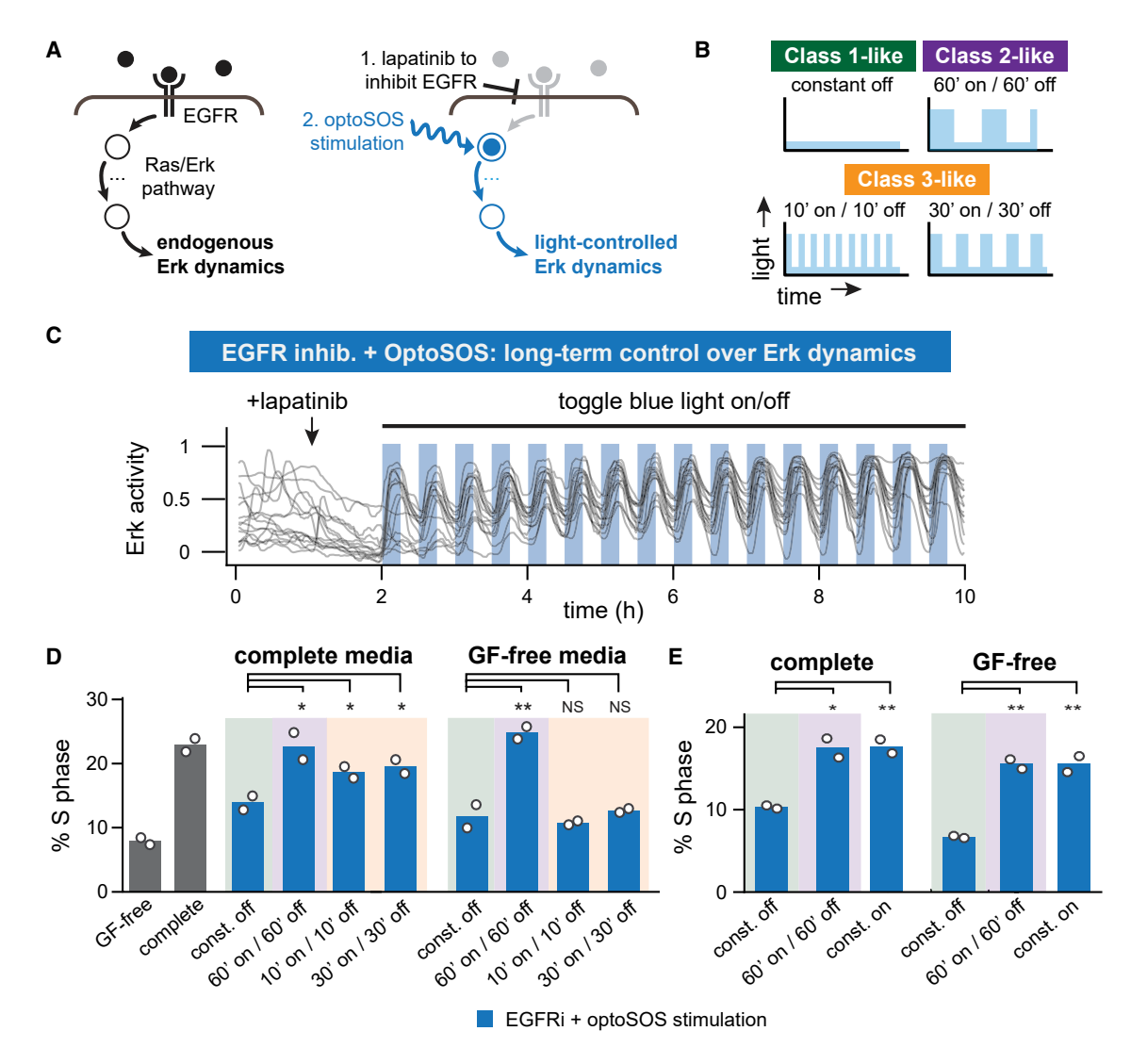


Figure 6. Direct Optogenetic Control over Erk Dynamics Reveals Drug-like Proliferative Responses

(A) Schematic of our strategy to implement direct optogenetic control in keratinocytes, which requires overriding their endogenous dynamics and establishing light-controlled Erk activity pulses. Endogenous Erk dynamics are first eliminated by treating cells with an EGFR inhibitor, then the OptoSOS system is used to apply light-dependent optogenetic inputs directly to Ras.

(B) Light pulses designed to mimic each class of drug-induced Erk dynamics: class 1-like suppression of Erk activity, class 2-like low-frequency pulses, or class 3-like high-frequency pulses.

(C) Representative single-cell Erk activity traces from keratinocytes stimulated as in A. Cells' endogenous dynamics were imaged for 1 h, then the EGFR inhibitor lapatinib was added to extinguish endogenous Erk signaling, after which blue light was toggled on and off every 15 min.

(D and E) Proliferation in response to optogenetic Erk stimulation mimicking class 1, 2, and 3 compounds (in D) or comparing pulsatile to continuous light stimulation (in E). Gray bars indicate control conditions: continuous GF-free media or complete media, both without lapatinib or light stimulation. Blue bars indicate OptoSOS keratinocytes treated with the EGFR inhibitor lapatinib, and then subjected to repeated blue light pulses at the schedules indicated. Green, purple, and orange shading indicate stimuli that drive Erk dynamics similar to class 1, 2, and 3 compounds, respectively. For all conditions, S phase entry was assessed after 22 h. Biological replicates (white circles) were assessed from flow cytometry DNA content distributions of at least 20,000 cells each. Statistics are derived using a one-sided t test (\*p < 0.05, \*\*p < 0.01, \*\*\*p < 0.001).

a 2-fold difference in overall dose (Figure 6E). Together, these results indicate that the change in Erk pulse duration is sufficient to explain the proliferative effects of our pharmacological classes, including the context dependence with which high-frequency Erk pulses drive proliferation in complete but not GF-free media. While we were initially surprised that keratinocytes could exhibit robust pulsatile Erk activity in GF-free media without proliferating, our data demonstrate that additional GF-dependent sig-

nals or longer-duration pulses are necessary to couple Erk activity to a proliferative response.

### **DISCUSSION**

Many signaling pathways exhibit complex, time-varying patterns of activity (Purvis and Lahav, 2013), yet in most cases it is unknown how these dynamics are generated, regulated, and

interpreted. Small-molecule and genetic screens could be powerful tools to better understand dynamics (Behar et al., 2013), as they have provided fundamental insights into the origins of complex phenotypes for over a century (Morgan, 1910; Nüsslein-Volhard and Wieschaus, 1980). However, the field is still only beginning to define how signaling dynamics screens should be designed and interpreted. One challenge is that dynamics can span many timescales, with pulses of activity that may rise or fall within minutes but occur only a few times per day (Albeck et al., 2013; Lahav et al., 2004; Nandagopal et al., 2018), necessitating minutes-timescale imaging over multi-day time periods. Dynamics can also be highly variable between cells and experimental conditions, requiring automated tracking and analysis of large numbers of cells to accurately estimate dynamic features.

Despite these challenges, we report a successful kinase inhibitor screen for altered Erk signaling dynamics. Our study relied on two crucial factors: an Erk biosensor whose activity can be quantified simply from measurements of nuclear fluorescence (Regot et al., 2014) and the discovery that primary keratinocytes harbor rapid, robust, and reproducible Erk dynamics in nearly all cells. Although few intracellular kinases are known to suppress MAPK signaling, our screen identified many kinase inhibitors that increased Erk activity, including a class of non-EGFR RTK inhibitors that increased the frequency of Erk pulses. We further defined the consequences of these altered Erk dynamics on cell proliferation, observing that IGF1-insulin receptor signaling is required for proliferation in response to the short, frequent Erk pulses observed in unstimulated cells or after class 3 drug treatment. In contrast, the low-frequency Erk pulses triggered by class 2 compounds were sufficient to trigger proliferation in the absence of additional cues. We anticipate that future studies will further define the molecular basis of cross talk between EGFR and non-EGFR RTKs, as well as the "decoding circuits" that initiate the cell's response to specific dynamics or combinations of intracellular pathways.

How might live-cell dynamic screens be extended and improved in future studies? The experimental design implemented here (450 experimental conditions analyzed over nine 5-h imaging sessions) is far from an upper limit and could be further increased by using a higher well density (e.g., 1,536 well plates) and a large field-of-view camera to capture multiple wells in a single image. More conditions could also be tested by reducing the total imaging time per stimulus or increasing the total number of imaging sessions. We anticipate that combining these improvements could increase overall throughput by 1-2 orders of magnitude, sufficient to screen ~10,000 conditions and open the door to genome-wide RNAi or CRISPR approaches (Wang et al., 2014). Merging live-cell imaging with genome-wide perturbation screening could profoundly transform our understanding of the molecular mechanisms driving intracellular signaling dynamics (Feldman et al., 2019).

### **STAR**\*METHODS

Detailed methods are provided in the online version of this paper and include the following:

- KEY RESOURCES TABLE
- LEAD CONTACT AND MATERIALS AVAILABILITY

- EXPERIMENTAL MODEL AND SUBJECT DETAILS
  - Cell Lines and Cell Culture
- METHOD DETAILS
  - Plasmids
  - O Lentivirus Production and Stable Transduction
  - Preparing Cells for Microscopy
  - Microscopy
  - Image Processing and Quantitative Analysis of Erk Dynamics
  - Optogenetics Experiments
  - Drug Treatments
  - Cell Lysate Collection and Western Blotting
  - Immunofluorescence Staining
  - Organotypic Keratinocyte Culture in Air-liquid Interface
  - O Proliferation and Cell Cycle Analysis
- QUANTIFICATION AND STATISTICAL ANALYSIS
- DATA AND CODE AVAILABILITY

#### SUPPLEMENTAL INFORMATION

Supplemental Information can be found online at https://doi.org/10.1016/j.cels.2020.02.005.

#### **ACKNOWLEDGMENTS**

We thank all members of the Toettcher and Devenport labs for their insights and comments. A.G.G. was supported by NIH Ruth L. Kirschstein NRSA fellowship F30CA206408. This work was also supported by NIH grant DP2EB024247 and NSF CAREER award 1750663 (to J.E.T.) and NIH training grant T32GM007388. We also thank Dr. Christina DeCoste and the Princeton Flow Cytometry Resource Center for flow cytometry support; Dr. Gary Laevsky and the Princeton Molecular Biology Microscopy Core, which is a Nikon Center of Excellence, for microscopy support; and Hahn Kim and the Princeton Small Molecule Screening Facility for support during the compound screen.

### **AUTHOR CONTRIBUTIONS**

A.G.G., M.Z.W., and J.E.T. conceived and designed the project. A.G.G., M.Z.W., and J.S. conducted the drug screen and analyzed data with J.E.T. A.G.G. and L.P.B. performed organotypic culture and tissue explant experiments. A.G.G. and S.G.J. performed supplementary drug stimulation experiments. A.G.G. performed all additional microscopy, cloning, and flow cytometry experiments. A.G.G. and J.E.T. wrote the paper, with editing from all authors. D.D. and J.E.T. provided funding and supervised the research.

### **DECLARATION OF INTERESTS**

The authors declare no competing interests.

Received: June 30, 2019 Revised: January 8, 2020 Accepted: February 24, 2020 Published: March 18, 2020

### **REFERENCES**

Abràmoff, M.D., Magalhães, P.J., and Ram, S.J.J.B.i. (2004). Image processing with ImageJ. Biophotonics international *11*, 36–42.

Albeck, J.G., Mills, G.B., and Brugge, J.S. (2013). Frequency-modulated pulses of ERK activity transmit quantitative proliferation signals. Mol. Cell *49*, 249–261.

Anastassiadis, T., Deacon, S.W., Devarajan, K., Ma, H., and Peterson, J.R. (2011). Comprehensive assay of kinase catalytic activity reveals features of kinase inhibitor selectivity. Nat. Biotechnol. *29*, 1039–1045.

Antczak, C., Mahida, J.P., Bhinder, B., Calder, P.A., and Djaballah, H. (2012). A high-content biosensor-based screen identifies cell-permeable activators and inhibitors of EGFR function: implications in drug discovery. J. Biomol. Screen. 17.885-899.

Aoki, K., Kondo, Y., Naoki, H., Hiratsuka, T., Itoh, R.E., and Matsuda, M. (2017). Propagating wave of ERK activation orients collective cell migration. Dev. Cell 43. 305-317.e5.

Aoki, K., Kumagai, Y., Sakurai, A., Komatsu, N., Fujita, Y., Shionyu, C., and Matsuda, M. (2013). Stochastic ERK activation induced by noise and cell-tocell propagation regulates cell density-dependent proliferation. Mol. Cell 52,

Aw, W.Y., Heck, B.W., Joyce, B., and Devenport, D. (2016). Transient tissuescale deformation coordinates alignment of planar cell polarity junctions in the mammalian skin. Curr. Biol. 26, 2090-2100.

Behar, M., Barken, D., Werner, S.L., and Hoffmann, A. (2013). The dynamics of signaling as a pharmacological target. Cell 155, 448-461.

Brand, T.M., Iida, M., Stein, A.P., Corrigan, K.L., Braverman, C.M., Luthar, N., Toulany, M., Gill, P.S., Salgia, R., Kimple, R.J., and Wheeler, D.L. (2014). AXL mediates resistance to cetuximab therapy. Cancer Res 74, 5152-5164.

Bugaj, L.J., Sabnis, A.J., Mitchell, A., Garbarino, J.E., Toettcher, J.E., Bivona, T.G., and Lim, W.A. (2018). Cancer mutations and targeted drugs can disrupt dynamic signal encoding by the Ras-Erk pathway. Science 361, https://doi. org/10.1126/science.aao3048.

Busch, H., Camacho-Trullio, D., Rogon, Z., Breuhahn, K., Angel, P., Eils, R., and Szabowski, A. (2008). Gene network dynamics controlling keratinocyte migration. Mol. Syst. Biol. 4, 199.

Chen, J.Y., Lin, J.R., Cimprich, K.A., and Meyer, T. (2012). A two-dimensional ERK-AKT signaling code for an NGF-triggered cell-fate decision. Mol. Cell 45, 196-209

Chmielowiec, J., Borowiak, M., Morkel, M., Stradal, T., Munz, B., Werner, S., Wehland, J., Birchmeier, C., and Birchmeier, W. (2007). c-Met is essential for wound healing in the skin. J. Cell Biol. 177, 151-162.

Darzynkiewicz, Z., and Juan, G. (2001). DNA content measurement for DNA ploidy and cell cycle analysis. Curr Protoc Cytom, 7.5.1-7.5.24.

de la Cova, C., Townley, R., Regot, S., and Greenwald, I. (2017). A Real-time biosensor for ERK activity reveals signaling dynamics during C. elegans cell fate specification. Dev. Cell 42, 542-553.e4.

Dine, E., Gil, A.A., Uribe, G., Brangwynne, C.P., and Toettcher, J.E. (2018). Protein Phase Separation Provides Long-Term Memory of Transient Spatial Stimuli. Cell Syst. 6, 655-663.e5.

Downward, J. (2001). The ins and outs of signalling. Nature 411, 759-762.

Engelman, J.A., Zejnullahu, K., Mitsudomi, T., Song, Y., Hyland, C., Park, J.O., Lindeman, N., Gale, C.M., Zhao, X., Christensen, J., et al. (2007). MET amplification leads to gefitinib resistance in lung cancer by activating ERBB3 signaling. Science 316, 1039-1043.

Feldman, D., Singh, A., Schmid-Burgk, J.L., Carlson, R.J., Mezger, A., Garrity, A.J., Zhang, F., and Blainey, P.C. (2019). Optical pooled screens in human cells. Cell 179, 787-799.e17.

Formisano, L., D'Amato, V., Servetto, A., Brillante, S., Raimondo, L., Di Mauro, C., Marciano, R., Orsini, R.C., Cosconati, S., Randazzo, A., et al. (2015). Src inhibitors act through different mechanisms in non-small cell lung cancer models depending on EGFR and RAS mutational status. Oncotarget 6, 26090-26103.

Gillies, T.E., Pargett, M., Minguet, M., Davies, A.E., and Albeck, J.G. (2017). Linear integration of ERK activity predominates over persistence detection in Fra-1 regulation. Cell Syst 5, 549-563.e5.

Giuliano, C.J., Lin, A., Smith, J.C., Palladino, A.C., and Sheltzer, J.M. (2018). MELK expression correlates with tumor mitotic activity but is not required for cancer growth. Elife 7, https://doi.org/10.7554/eLife.32838.

Goglia, A.G., Wilson, M.Z., DiGiorno, D.B., and Toettcher, J.E. (2017). Optogenetic control of Ras/erk signaling using the Phy-PIF system. Methods Mol. Biol. 1636, 3-20.

Guntas, G., Hallett, R.A., Zimmerman, S.P., Williams, T., Yumerefendi, H., Bear, J.E., and Kuhlman, B. (2015). Engineering an improved light-induced

dimer (iLID) for controlling the localization and activity of signaling proteins. Proc. Natl. Acad. Sci. USA 112. 112-117.

Hall-Jackson, C.A., Eyers, P.A., Cohen, P., Goedert, M., Boyle, F.T., Hewitt, N., Plant, H., and Hedge, P. (1999). Paradoxical activation of Raf by a novel Raf inhibitor Chem Biol 6, 559-568.

Hamstra, D.A., Bhojani, M.S., Griffin, L.B., Laxman, B., Ross, B.D., and Rehemtulla, A. (2006). Real-time evaluation of p53 oscillatory behavior in vivo using bioluminescent imaging. Cancer Res 66, 7482-7489.

Hatzivassiliou, G., Song, K., Yen, I., Brandhuber, B.J., Anderson, D.J., Alvarado, R., Ludlam, M.J., Stokoe, D., Gloor, S.L., Vigers, G., et al. (2010). RAF inhibitors prime wild-type RAF to activate the MAPK pathway and enhance growth. Nature 464, 431-435.

Heidorn, S.J., Milagre, C., Whittaker, S., Nourry, A., Niculescu-Duvas, I., Dhomen, N., Hussain, J., Reis-Filho, J.S., Springer, C.J., Pritchard, C., and Marais, R. (2010). Kinase-dead BRAF and oncogenic RAS cooperate to drive tumor progression through CRAF. Cell 140, 209-221.

Hiratsuka, T., Fujita, Y., Naoki, H., Aoki, K., Kamioka, Y., and Matsuda, M. (2015). Intercellular propagation of extracellular signal-regulated kinase activation revealed by in vivo imaging of mouse skin. Elife 4, e05178.

Hoeller, O., Toettcher, J.E., Cai, H., Sun, Y., Huang, C.H., Freyre, M., Zhao, M., Devreotes, P.N., and Weiner, O.D. (2016). Gbeta regulates coupling between actin oscillators for cell polarity and directional migration. PLoS Biol 14, e1002381.

Janes, K.A., Wang, C.C., Holmberg, K.J., Cabral, K., and Brugge, J.S. (2010). Identifying single-cell molecular programs by stochastic profiling. Nat. Methods 7, 311-317.

Jaqaman, K., Loerke, D., Mettlen, M., Kuwata, H., Grinstein, S., Schmid, S.L., and Danuser, G. (2008). Robust single-particle tracking in live-cell time-lapse sequences. Nat. Methods 5, 695-702.

Johnson, H.E., Goyal, Y., Pannucci, N.L., Schüpbach, T., Shvartsman, S.Y., and Toettcher, J.E. (2017). The spatiotemporal limits of developmental erk signaling. Dev. Cell 40, 185-192.

Johnson, H.E., and Toettcher, J.E. (2019). Signaling dynamics control cell fate in the early Drosophila embryo. Dev. Cell 48, 361-370.e3.

Joslin, E.J., Shankaran, H., Opresko, L.K., Bollinger, N., Lauffenburger, D.A., and Wiley, H.S. (2010). Structure of the EGF receptor transactivation circuit integrates multiple signals with cell context. Mol. Biosyst. 6, 1293-1306.

Karaman, M.W., Herrgard, S., Treiber, D.K., Gallant, P., Atteridge, C.E., Campbell, B.T., Chan, K.W., Ciceri, P., Davis, M.I., Edeen, P.T., et al. (2008). A quantitative analysis of kinase inhibitor selectivity. Nat. Biotechnol. 26,

Keenan, A.B., Jenkins, S.L., Jagodnik, K.M., Koplev, S., He, E., Torre, D., Wang, Z., Dohlman, A.B., Silverstein, M.C., Lachmann, A., et al. (2018). The Library of Integrated network-based cellular signatures NIH program: system-level cataloging of human cells response to perturbations. Cell Syst 6. 13-24.

Krall, J.A., Beyer, E.M., and MacBeath, G. (2011). High- and low-affinity epidermal growth factor receptor-ligand interactions activate distinct signaling pathways. PLoS One 6, e15945.

Lahav, G., Rosenfeld, N., Sigal, A., Geva-Zatorsky, N., Levine, A.J., Elowitz, M.B., and Alon, U. (2004). Dynamics of the p53-Mdm2 feedback loop in individual cells. Nat. Genet. 36, 147-150.

Lemmon, M.A., and Schlessinger, J. (2010). Cell signaling by receptor tyrosine kinases, Cell 141, 1117-1134.

Locatelli, A., and Lange, C.A. (2011). Met receptors induce Sam68-dependent cell migration by activation of alternate extracellular signal-regulated kinase family members. J. Biol. Chem. 286, 21062-21072.

Man, X.Y., Yang, X.H., Cai, S.Q., Bu, Z.Y., and Zheng, M. (2008). Overexpression of vascular endothelial growth factor (VEGF) receptors on keratinocytes in psoriasis: regulated by calcium independent of VEGF. J. Cell. Mol. Med. 12, 649-660.

Man, X.Y., Yang, X.H., Cai, S.Q., Yao, Y.G., and Zheng, M. (2006). Immunolocalization and expression of vascular endothelial growth factor receptors (VEGFRs) and neuropilins (NRPs) on keratinocytes in human epidermis. Mol. Med. 12, 127–136.

Marshall, C.J. (1995). Specificity of receptor tyrosine kinase signaling: transient versus sustained extracellular signal-regulated kinase activation. Cell 80, 179–185.

Mendoza, M.C., Er, E.E., and Blenis, J. (2011). The Ras-ERK and PI3K-mTOR pathways: cross-talk and compensation. Trends Biochem. Sci. 36, 320–328.

Miyamoto, K., and Sawa, M. (2019). Development of highly sensitive biosensors of RAF dimerization in cells. Sci. Rep. 9, 636.

Moret, N., Clark, N.A., Hafner, M., Wang, Y., Lounkine, E., Medvedovic, M., Wang, J., Gray, N., Jenkins, J., and Sorger, P.K. (2019). Cheminformatics tools for analyzing and designing optimized small-molecule collections and libraries. Cell Chem. Biol. 26, 765–777.e3.

Morgan, T.H. (1910). Sex limited inheritance in Drosophila. Science 32, 120–122

Nandagopal, N., Santat, L.A., LeBon, L., Sprinzak, D., Bronner, M.E., and Elowitz, M.B. (2018). Dynamic ligand discrimination in the Notch signaling pathway. Cell 172, 869–880.e19.

Niopek, D., Wehler, P., Roensch, J., Eils, R., and Di Ventura, B. (2016). Optogenetic control of nuclear protein export. Nat. Commun. 7, 10624.

Nowak, J.A., and Fuchs, E. (2009). Isolation and culture of epithelial stem cells. Methods Mol. Biol. 482, 215–232.

Nüsslein-Volhard, C., and Wieschaus, E. (1980). Mutations affecting segment number and polarity in Drosophila. Nature 287, 795–801.

Pinilla-Macua, I., Grassart, A., Duvvuri, U., Watkins, S.C., and Sorkin, A. (2017). EGF receptor signaling, phosphorylation, ubiquitylation and endocytosis in tumors in vivo. Elife *6*, https://doi.org/10.7554/eLife.31993.

Poulikakos, P.I., Zhang, C., Bollag, G., Shokat, K.M., and Rosen, N. (2010). RAF inhibitors transactivate RAF dimers and ERK signalling in cells with wild-type BRAF. Nature 464, 427–430.

Purvis, J.E., and Lahav, G. (2013). Encoding and decoding cellular information through signaling dynamics. Cell *152*, 945–956.

Regot, S., Hughey, J.J., Bajar, B.T., Carrasco, S., and Covert, M.W. (2014). High-sensitivity measurements of multiple kinase activities in live single cells. Cell 157, 1724–1734

Schindelin, J., Araganda-Carreras, I., Frise, E., Kaynig, V., Longair, M., Pietzsch, T., Preibisch, S., Rueden, C., Saalfeld, S., Schmid, B., et al. (2012).

Fiji: an open-source platform for biological-image analysis. Nat. Methods 9, 676–682

Shankaran, H., Ippolito, D.L., Chrisler, W.B., Resat, H., Bollinger, N., Opresko, L.K., and Wiley, H.S. (2009). Rapid and sustained nuclear-cytoplasmic ERK oscillations induced by epidermal growth factor. Mol. Syst. Biol. 5, 332.

Stewart-Ornstein, J., and Lahav, G. (2017). p53 dynamics in response to DNA damage vary across cell lines and are shaped by efficiency of DNA repair and activity of the kinase ATM. Sci. Signal. 10, https://doi.org/10.1126/scisignal.aah6671.

Tinevez, J.Y., Perry, N., Schindelin, J., Hoopes, G.M., Reynolds, G.D., Laplantine, E., Bednarek, S.Y., Shorte, S.L., and Eliceiri, K.W. (2017). TrackMate: an open and extensible platform for single-particle tracking. Methods *115*, 80–90.

Toettcher, J.E., Weiner, O.D., and Lim, W.A. (2013). Using optogenetics to interrogate the dynamic control of signal transmission by the Ras/Erk module. Cell *155*, 1422–1434.

Wang, T., Wei, J.J., Sabatini, D.M., and Lander, E.S. (2014). Genetic screens in human cells using the CRISPR-Cas9 system. Science 343, 80–84.

Waters, K.M., Cummings, B.S., Shankaran, H., Scholpa, N.E., and Weber, T.J. (2014). ERK oscillation-dependent gene expression patterns and deregulation by stress response. Chem. Res. Toxicol. 27, 1496–1503.

Wilgus, T.A., Matthies, A.M., Radek, K.A., Dovi, J.V., Burns, A.L., Shankar, R., and DiPietro, L.A. (2005). Novel function for vascular endothelial growth factor receptor-1 on epidermal keratinocytes. Am. J. Pathol. *167*, 1257–1266.

Wu, X.J., Zhu, J.W., Jing, J., Xue, D., Liu, H., Zheng, M., and Lu, Z.F. (2014). VEGF165 modulates proliferation, adhesion, migration and differentiation of cultured human outer root sheath cells from central hair follicle epithelium through VEGFR-2 activation in vitro. J. Dermatol. Sci. 73, 152–160.

Zetterberg, A., and Larsson, O. (1985). Kinetic analysis of regulatory events in G1 leading to proliferation or quiescence of Swiss 3T3 cells. Proc. Natl. Acad. Sci. USA 82, 5365–5369.

Zufferey, R., Dull, T., Mandel, R.J., Bukovsky, A., Quiroz, D., Naldini, L., and Trono, D. (1998). Self-inactivating lentivirus vector for safe and efficient in vivo gene delivery. J. Virol. 72, 9873–9880.

Zwang, Y., Sas-Chen, A., Drier, Y., Shay, T., Avraham, R., Lauriola, M., Shema, E., Lidor-Nili, E., Jacob-Hirsch, J., Amariglio, N., et al. (2011). Two phases of mitogenic signaling unveil roles for p53 and EGR1 in elimination of inconsistent growth signals. Mol. Cell 42, 524–535.

### **STAR**\***METHODS**

### **KEY RESOURCES TABLE**

REAGENT or RESOURCE	SOURCE	IDENTIFIER
Antibodies		
Total Erk 1/2 mouse antibody	Cell Signaling Technologies	Cat# 4696; RRID:AB_390780
Phospho-Erk 1/2 rabbit antibody	Cell Signaling Technologies	Cat# 4370; RRID:AB_2315112
Phospho-EGFR rabbit antibody	Cell Signaling Technologies	Cat# 3777; RRID:AB_2096270
β-actin mouse antibody	Cell Signaling Technologies	Cat# 3700; RRID:AB_2242334
Phospho-Akt rabbit antibody	Cell Signaling Technologies	Cat# 4060; RRID:AB_2315049
Total Akt mouse antibody	Cell Signaling Technologies	Cat# 2920; RRID:AB_1147620
Bacterial and Virus Strains		
Stellar Chemically Competent Cells	ClonTech Laboratories	Cat# 636763
Chemicals, Peptides, and Recombinant Proteins		
Actinomycin D	Sigma-Aldrich	Cat# A1410
Cabozantinib	SelleckChem	Cat# S1119
Chelex 100 Resin	Bio-Rad	Cat# 142-2842
Cholera Toxin	Sigma-Aldrich	Cat# C8052
CloneAmp HiFi PCR Polymerase	ClonTech Laboratories	Cat# 639298
cOmplete, Mini, EDTA-free Protease Inhibitor Cocktail	Sigma-Aldrich	Cat# 11836170001
DMEM/F12 (3:1) without calcium	Life Technologies	Cat# 90-5010
Epidermal growth factor (EGF)	R&D Systems	Cat# 3214-EG-100
FuGENE HD	Promega	Cat# E2311
GDC0879	SelleckChem	Cat# S1104
Hydrocortisone	Sigma-Aldrich	Cat# H0888
nFusion HD Cloning Kit	ClonTech Laboratories	Cat# 638911
nsulin, recombinant	Sigma-Aldrich	Cat# 91077C
_apatinib	SelleckChem	Cat# S2111
NuPAGE LDS Sample Buffer	Thermo-Fisher	Cat# NP0007
Pazopanib	SelleckChem	Cat# S3012
Pictilisib (GDC-0941)	SelleckChem	Cat# S1065
PhosSTOP	Sigma-Aldrich	Cat# 4906837001
Polybrene	Sigma-Aldrich	Cat# 107689
Puromycin dihydrochloride (Puromycin)	Sigma-Aldrich	Cat# P8833
SB590885	SelleckChem	Cat# S2220
SelleckChem Kinase Inhibitor Library	SelleckChem	Cat# L1200
Sodium Bicarbonate	Sigma-Aldrich	Cat# S5761
T3 (3,3',5-triiodo-L-thyronine)	Sigma-Aldrich	Cat# T2877
TAPI-1	SelleckChem	Cat# S7434
Tivozanib	SelleckChem	Cat# S1207
Transferrin	Sigma-Aldrich	Cat# T2252
Deposited Data		
Raw/analyzed microscopy data from the nhibitor screen (Figure 3)	This paper	idr.openmicroscopy.org/; accession # idr0064
Experimental Models: Cell Lines		
CD-1 mouse primary keratinocytes	This paper; Danelle Devenport, Princeton University	N/A
ErkKTR-BFP::H2B-RFP (CD-1 mouse primary keratinocytes)	This paper	N/A
, ,		(Continued on next

(Continued on next page)

Continued			
REAGENT or RESOURCE	SOURCE	IDENTIFIER	
ErkKTR-BFP::H2B-RFP::BFP-SSPB- SOScat-2A-PuroR-2A-iLID-CAAX (CD-1 mouse primary keratinocytes)	This paper	N/A	
BFP-SSPB-SOScat-2A-PuroR-2A-iLID- CAAX (CD1 primary mouse keratinocytes)	This paper	N/A	
iRFP-LEXY (CD1 primary mouse keratinocytes)	This paper	N/A	
Lenti-X HEK 293T cells	ClonTech Laboratories	Cat# 632180	
MCF10A human breast epithelial cells, clone 5E	Joan Brugge, Harvard Medical School (Janes et al., 2010)	RRID:CVCL_0598	
ErkKTR-iRFP-2A-H2B-RFP (MCF10A, clone 5E)	This paper	N/A	
Recombinant DNA			
pHR SFFVp ErkKTR-BFP	This paper, Regot et al., 2014	Addgene # forthcoming	
pHR SFFVp BFP-SSPB-SOScat-2A-PuroR- 2A-iLID-CAAX	This paper, Johnson et al., 2017	Addgene # forthcoming	
pHR iRFP-LEXY CONSTRUCT	This paper, Niopek et al., 2016	Addgene # forthcoming	
pHR SFFVp ErkKTR-iRFP	Dine et al., 2018	Addgene #111510	
H2B-tagRFP	Gift from Philip Keller	Addgene #99271	
pCMV-dR8.91 lentivirus packaging plasmid	Gift from the Trono lab	N/A	
pMD2.G lentivirus envelope plasmid	Gift from the Trono lab	Addgene #12259	
Software and Algorithms			
Fiji	Schindelin et al., 2012	http://fiji.sc, RRID: SCR_002285	
MATLAB	Mathworks	SCR_001622	
NIS-Elements AR	Nikon	RRID:SCR_014329	
TrackMate	Jaqaman et al., 2008; Tinevez et al., 2017	https://imagej.net/TrackMate	
Jython analysis code	This paper	github.com/toettchlab/Goglia2019	
MATLAB analysis code	This paper	github.com/toettchlab/Goglia2019	

### LEAD CONTACT AND MATERIALS AVAILABILITY

Further information and requests for resources and reagents should be directed to and will be fulfilled by the Lead Contact, Jared Toettcher (toettcher@princeton.edu). This study did not generate new reagents.

### **EXPERIMENTAL MODEL AND SUBJECT DETAILS**

### **Cell Lines and Cell Culture**

Dorsal epidermal keratinocytes derived from CD1 mice and stably expressing a retrovirally-delivered histone H2B-RFP (selected for expression with hygromycin) were obtained from the Devenport lab (B. Heck) and were cultured as described previously (Nowak and Fuchs, 2009). Briefly, keratinocytes were grown in complete low calcium (50  $\mu$ M) growth media ('E media' supplemented with 15% serum and 0.05 mM Ca<sup>2+</sup>) in Nunc Cell Culture Treated Flasks with filter caps (Thermo) and were maintained in a humidified incubator at 37° C with 5% CO<sub>2</sub>. Cell passage number was kept below 30. Keratinocyte media was prepared as per (Nowak and Fuchs, 2009), except as indicated in the text and Table S2.

### **METHOD DETAILS**

### **Plasmids**

The pHR backbone (Addgene #79121) was used for all lentiviral expression constructs (Zufferey et al., 1998). All constructs were cloned using PCR amplification of complementary fragments and In-Fusion HD-based assembly (Takara). ErkKTR-BFP was cloned by PCR amplification of TagBFP (Addgene #102350) and insertion into the pHR ErkKTR-iRFP construct used previously (Addgene #111510). BFP-SSPB-SOScat-2A-PuroR-2A-iLID-CAAX was cloned from the pTiger-OptoSOS construct used previously (Addgene #86439), followed by PCR amplification and insertion of 2A-PuroR (a gift from Brett Stringer; Addgene #98290) and TagBFP. ErkKTR-iRFP-2A-H2B-tRFP was cloned by PCR amplification of the 2A cleavage site from pTiger-OptoSOS and amplification of

the H2B-tagRFP coding sequence (a gift from Sergi Regot and Philipp Keller; Addgene # 99271), followed by insertion into pHR ErkKTR-iRFP. H2B-RFP retrovirus was previously constructed in the Devenport lab (B. Heck) using the pSINRevPGK-hyg backbone (S. Williams, Elaine Fuchs lab). The pHR irFP-LEXY plasmid was constructed using the LEXY sequence (Addgene plasmid # 72655) and irFP sequences (Addgene plasmid # 111510) by PCR amplification and inserted into the pHR backbone.

#### **Lentivirus Production and Stable Transduction**

Lentivirus was generated as described previously (Goglia et al., 2017). Briefly, Lenti-X HEK293T cells were seeded at roughly 50% confluency in 6-well dishes. Cells were allowed to settle for 12 h, after which FuGENE HD transfection reagent was used to co-transfect cells with the desired pHR expression vector and the two necessary lentivirus helper plasmids (pCMV-dR8.91 and pMD2.G – gifts from the Trono lab). Viral supernatants were collected 48-52 h after transfection, cell debris was removed using a 0.45  $\mu$ m filter, and viruses were either used immediately or stored at -80° C.

For viral transduction, keratinocytes were plated at <50% confluency in 6-well dishes, allowed to adhere overnight, and then treated with 100  $\mu$ L of the desired lentivirus. Viral supernatants were supplemented with 5  $\mu$ g/mL Polybrene and 50  $\mu$ M HEPES buffer. Virus-containing media was removed after 24 h and cells were transferred into new tissue culture flasks. Fluorescence-activated cell sorting (FACS) was used to isolate keratinocytes that stably expressed both high levels of the H2B-RFP nuclear marker and low levels of the ErkKTR-BFP reporter. Sorting was performed using a FACSAriallI Fusion system with 355, 405, 488, 561, and 637 nm laser excitation sources (BD Biosciences).

For optogenetic experiments, a separate line of OptoSOS keratinocytes was generated using the same lentiviral transduction procedures outlined above and then, 3d after transduction, selecting for expression by exposing cells to puromycin (2  $\mu$ g/mL) for > 3d. Sorted/selected cells were then expanded into multiple large culture flasks and 20 vials of each sorted line were frozen down and stored in liquid nitrogen for use during the study.

### **Preparing Cells for Microscopy**

Imaging experiments were performed in either 384- or 96-well black-walled, 0.17mm high performance glass-bottom plates (Cellvis). Before plating, the bottom of each well was pre-treated with a solution of 10  $\mu$ g/mL bovine plasma fibronectin (Thermo Fisher) in phosphate buffered saline (PBS) to support cell adherence. Two days before imaging, keratinocytes were seeded at 16,000 cells/well in 50  $\mu$ L of low-calcium E media (in a 384-well plate), plates were briefly centrifuged at 100  $\times$  g to ensure even plating distribution, and cells were allowed to adhere overnight. 24 h before imaging, wells were washed 2-3X with PBS to remove non-adherent cells and were shifted to high-calcium (1.5 mM CaCl<sub>2</sub>) complete E media to promote epithelial monolayer formation. For experiments in GF-free media, cells were washed once with PBS and shifted to high-calcium P media (i.e., DMEM/F12 containing only pH buffer, penicillin/streptomycin, and 1.5 mM CaCl<sub>2</sub>) eight hours before imaging. To prevent evaporation during time-lapse imaging, a 50  $\mu$ L layer of mineral oil was added to the top of each well immediately before imaging.

The kinase inhibitor library was screened in rounds of 48 drugs plus two DMSO controls per plate for a total of 50 wells, as this was the maximum number of conditions that could be imaged every 3 min in two fluorescent channels. Thus, nine initial rounds of imaging were required to screen all 429 drugs in the library. Cell plating was staggered such that a fresh plate of 50 wells in GF-free media was ready to be imaged every 8 h. An additional two rounds were added to re-screen drugs from wells with insufficient cell density.

### **Microscopy**

Imaging was performed on a Nikon Eclipse Ti confocal microscope, with a Yokogawa CSU-X1 spinning disk, a Prior Proscan III motorized stage, an Agilent MLC 400B laser launch containing 405, 488, 561, and 650 nm lasers, a cooled iXon DU897 EMCCD camera, and fitted with an environmental chamber to ensure cells were kept at a  $37^{\circ}$  C and 5% CO<sub>2</sub> during imaging. All images were captured with either a 10X or 20X air objective and were collected at intervals of 2-3 min.

# Image Processing and Quantitative Analysis of Erk Dynamics Processing Raw TIFF Files into Tracked/Segmented Erk Activity Dynamics

Our analysis pipeline takes as input a two-color, multi-timepoint TIFF stack that includes two fluorescent channels – KTR-BFP and H2B-RFP – for monitoring Erk activity and tracking/segmenting nuclei. These TIFF images contained metadata including the spatial scale of the data, and since our analysis pipeline incorporates true spatial units (µm rather than pixels), it can be used for images collected with any objective magnification. We first used a FIJI Jython script batch\_trackmate.py to automatically run the TrackMate segmentation/tracking plugin (Jaqaman et al., 2008; Tinevez et al., 2017) on a folder of TIFF stacks, returning the mean nuclear intensity for each cell in both the H2B and KTR channels. Each dataset thus consisted of two paired folders: one containing all the TIFFs (with names <image\_name>.tif) and one of the corresponding TrackMate tracks (with names <image\_name>.txt). In addition to containing the mean nuclear intensities in all fluorescent channels, the resulting TrackMate tracks also include the X-Y locations of each nucleus at all timepoints, enabling analysis of each cell's overall displacement and velocity.

### **Analyzing Erk Activity Dynamics from Tracked Cells**

All subsequent analyses were performed in MATLAB. We wrote a set of analysis tools to automatically load the TIFFs and TrackMate tracks from the paired folders and analyze them with a set of options specified in a comma-delimited parameters file that is generated for each dataset. We first exclude TrackMate-tracked nuclei on either of two conditions: (1) they do not express both H2B and KTR, or (2) if H2B intensity changes dramatically over the imaging timecourse, indicating a tracking error (Figures S1A and S1B). We then filter

and process nuclear KTR intensities using the following steps: (1) data is background-subtracted; (2) data is h-minima transformed to 'flatten' noise between consecutive timepoints; (3) data is inverted and scaled assuming that the maximum nuclear KTR intensity observed for each cell corresponds to Erk activity of 0; and (4) data is fed into a peak-finding routine that splits the trajectory into windows containing individual peaks, which are then analyzed using MATLAB's built-in findpeaks.m function (Figures S1C and S1D).

#### Estimating the Overall Erk Activity Offset for the Entire Well

In addition to analysis of single-cell trajectories, we also perform one well-averaged measurement at each timepoint: the overall cytosol-to-nuclear ratio computed for all identified cells. To do so, we used image dilation and erosion operations to obtain an annulus of cytoplasm surrounding all segmented nuclei. We then computed the mean C/N ratio by measuring the mean intensity in all cytosolic pixels divided by the mean intensity of all nuclear pixels (Figures S1E and S1F). We found this ratio to be an excellent proxy for well-averaged activity; as an example, it is able to accurately detect keratinocytes' graded Erk responses to increasing doses of EGF (Figure S1G). We opted for a well-averaged C/N ratio rather than a single-cell ratio primarily because correctly assigning cytosolic regions to the appropriate nucleus can be quite tricky, especially in an epithelial monolayer.

At the conclusion of our analysis routine, the user is provided with two data structures: well, which contains the raw and processed nuclear KTR and Erk activity trajectories; and PS, a structure that contains all analyses of Erk dynamics over time (e.g., frequency, pulse prominence, overall Erk activity offset, total distance moved per cell, etc.). These quantities were used for all subsequent analyses. Example runs are available on Github (github.com/toettchlab/Goglia2019).

### **Optogenetics Experiments**

For microscopy experiments involving optogenetic stimulation, an X-Cite XLED1 light source coupled to a Polygon400 Mightex Systems digital micromirror device (DMD) was used to stimulate cells with saturating doses of 450 nm blue light that were applied for 500 ms every 1 min (for OptoSOS) or every 15 sec (for LEXY).

For proliferation experiments involving optogenetic stimuli, light was delivered using custom-printed circuit boards of blue 450 nm light-emitting diodes (LEDs). During light stimulation, cells were maintained in an incubator at 37° C in separate foil-wrapped boxes covered with separate blue LED boards delivering different patterns of light inputs. Each LED board was connected to a separate constant-current LED driver, all of which were controlled using an Arduino MEGA 2560 microcontroller board. The Arduino was programmed with open-source IDE software to deliver different dynamic light input regimes to each circuit board. To minimize phototoxicity, light inputs were delivered in cycles of 10 sec ON and 20 sec OFF – this allowed us to minimize light exposure while still delivering a constant stimulus to cells by taking advantage of the slow ( $\sim$  0.5–1 min) dark decay rate of iLID activation (Guntas et al., 2015).

# **Drug Treatments Drug Screen**

An Echo® acoustic liquid handler (Labcyte) was used to precisely spot plastic 96-well plates with 75 nL of either DMSO vehicle control or of individual drugs from the kinase inhibitor library (Selleck Chem). 100  $\mu$ L of P media was then added to each well that had been spotted by the Echo to create 3X stock solutions that could be rapidly added to plates of cells by multi-channel pipetting. Keratinocytes were plated on glass 384-well dishes in 50  $\mu$ L of media and a final drug concentration of 2.5  $\mu$ M was achieved by adding 25  $\mu$ L of each 3X stock solution to individual wells of keratinocytes. Imaging was carried out 30 min after drug additions.

### Subsequent Testing of Class 1, 2, and 3 Hits

After downstream analyses of the primary screen, new aliquots of all top drug hits were purchased from Selleck Chemicals and drug effects were confirmed via extended time-lapse imaging. For all subsequent experiments involving confirmed drug hits (e.g., individual drug follow-ups, proliferation assays), drug additions were performed by first creating a 10X working stock by diluting drug/growth factor/neutralizing antibody in GF-free media and then adding an appropriate volume of this stock to cultured cells.

### **Determining EGFR-dependence of Class 3 Drug Effects**

KTR-H2B keratinocytes were prepared for imaging in multi-well plates as before. Prior to imaging, half the wells were pre-treated with the EGFR inhibitor lapatinib at  $2.5~\mu\text{M}$  while the other half were given a DMSO vehicle control and Erk dynamics were monitored by time-lapse confocal microscopy. After 1 h of imaging, representative Class 2 and Class 3 compounds were added to either DMSO- or lapatinib-pre-treated cells and the resulting Erk dynamics were monitored over 8 h.

### Assessing Transcription-dependence of Endogenous Erk Activity Pulses

KTR-H2B keratinocytes were prepared for imaging in multi-well plates as before. After 1 h of imaging, cells were either treated with the transcription inhibitor actinomycin D at 5  $\mu$ g/mL or with DMSO vehicle control. Cells were imaged every 2 min for a total of 6 h.

### Assessing MMP- and ADAM-dependence of Endogenous Erk Activity Pulses

KTR-H2B keratinocytes were prepared for imaging in multi-well plates as before. After 10 min of imaging, either DMSO vehicle control or TAPI-1 was added at the indicated concentrations. Cells were imaged every 2 min for 12 h.

### Assessing MMP- and ADAM-dependence of Erk Dynamics-altering Drug Hits

KTR-H2B keratinocytes were prepared for imaging in multi-well plates as before. After 10 min of imaging, either DMSO vehicle control or TAPI-1 was added at 10  $\mu$ M. After 3 h of imaging, either DMSO or a representative Class 2 or Class 3 compound was added. Cells were imaged every 2 min for 14 h.

### **Cell Lysate Collection and Western Blotting**

### Time Course of Drug-induced EGFR and Erk Phosphorylation

Two days before lysate collection, cells were seeded at 3 × 10<sup>6</sup> in 6-well tissue culture dishes and allowed to adhere overnight. 24 h before collection, cells were washed 3X with PBS and shifted to high-calcium media to promote epithelial monolayer formation. Drugs/growth factors were added to cells at the indicated times before lysate collection (all drugs added at 2.5 μM; EGF added at 10 ng/mL). At indicated time points, media was aspirated, cells were washed with PBS and were lysed with 100 μL of ice-cold RPPA buffer (1% Triton X-100, 50 mM HEPES buffer, 150 mM NaCl, 1.5 mM MgCl<sub>2</sub>, 1 mM EGTA, 100 mM NaF, 10 mM sodium pyrophosphate, 1 mM Na<sub>3</sub>VO<sub>4</sub>, 10% glycerol, freshly-prepared protease/phosphatase inhibitors). Cell scrapers were used to remove cells from the surface of each well, then each lysate was transferred to an ice-cold Eppendorf tube and centrifuged at 17,000 x g for 10 min at 4° C. Supernatants were transferred to new tubes, 25 µL of 4X NuPAGE LDS Sample Buffer (Thermo Fisher) was added to each, and samples were boiled at 98° C for 5 min. Samples were then stored at -80° C.

For Western blotting, lysates were run in 17-well 4-12% Bis-Tris gels (Thermo Fisher) at 120V for 1.5 h. A Trans-Blot SD semi-dry transfer cell (Bio-Rad) was used to transfer protein samples from gels to nitrocellulose membranes. Single-gel transfers were run at constant current of 70mA and max voltage of 25V for 1 h. Nitrocellulose membranes were then blocked for 1 h at room temperature in Odyssey blocking buffer (Li-Cor) and were incubated overnight at 4° C on a plate rocker in a 1:1000 dilution of primary antibody in blocking buffer. The following antibodies were used: anti-phospho-Erk1/2 rabbit monoclonal antibody (Cell Signaling #4370), antiphospho-EGFR (pY1068) rabbit monoclonal antibody (Cell Signaling #3777), and anti-total-Erk1/2 mouse monoclonal antibody (Cell Signaling #4696). The next day, blots were washed 5 × 5 min with TBST and then incubated for 1 h at room temperature in a 1:10,000 dilution of IRDye 680RD goat anti-mouse and 800CW goat anti-rabbit fluorescent secondary antibodies (Li-Cor). Blots were then washed 5 x 5 min with TBST, imaged on a Li-Cor Odyssey CLx imaging system, and images were analyzed using Image Studio software (Li-Cor).

### EGFR and Erk Phosphorylation in Keratinocytes Treated with Increasing Doses of EGF

Keratinocytes were plated and prepared for lysate collection as described above. EGF was added to cells for 15 min, after which cells were lysed and collected as above. Western blotting was performed as above and blots were probed for phospho-Erk1/2 (Cell Signaling #4370), phospho-EGFR (pY1068) (Cell Signaling #3777), and β-actin (mouse monoclonal antibody; Cell Signaling #3700). Blots were imaged and analyzed as above.

### Assessing the Effects of Drug Screen Hits on PI3K/Akt Pathway Activation

Keratinocytes were plated and prepared as above. Drugs/growth factors were added to cells 1 h before lysate collection (all drugs added at 2.5 µM; EGF added at 10 ng/mL). Western blotting and imaging were performed as above, with blots probed for phospho-Akt (pS473) (Cell Signaling #4060), total Akt (Cell Signaling #2920), and total-Erk1/2 (Cell Signaling #4696). Subsequent imaging and analyses were performed as above.

### **Immunofluorescence Staining**

E14.5 embryos were dissected in PBS and fixed with 4% paraformaldehyde for 1 h. Dissected back skins were washed 3 × 5 min with PBS and then placed in permeabilization / blocking buffer (0.3% Triton X-100, 2% normal goat serum, 2% normal donkey serum, 2% bovine serum albumin, and 1% fish gelatin in PBS) for 2 h at room temperature. Samples were then incubated overnight on a plate rocker at 4° C in a 1:200 dilution of anti-phospho-Erk1/2 (Thr202/Tyr204) rabbit monoclonal antibody (Cell Signaling #4370) in blocking buffer. The next morning, samples were washed 3 × 30 min with blocking buffer and then incubated for 2 h at room temperature in a 1:750 dilution of Alexa Fluor 488-conjugated donkey anti-rabbit secondary antibody (Thermo Fisher A21206) and 1 µg/mL DAPI in blocking buffer. Tissues were again washed 3 × 30 min with blocking buffer, mounted on coverslips in Fluoro-Gel mounting medium (Electron Microscopy Sciences, Cat. # 17985-30), and imaged by confocal microscopy.

### Organotypic Keratinocyte Culture in Air-liquid Interface

500,000 primary KTR-H2B keratinocytes were seeded on inverted 1.1 cm<sup>2</sup> hanging cell culture inserts fit with 0.4 μm pore polyethylene terephthalate (PET) filters (Millipore PIHT15R48) in high calcium E media (1.5 mM). For the first 3 days, cells were grown with media on either side of the filter and were provided with fresh media daily. An air-liquid interface (ALI) was established on day three by removing all media, inverting the cell culture insert to hang in a 24-well dish, and then replacing media only inside the cell culture insert (i.e., removing media from above the cells) (Figure S2F). Cells were grown in ALI for an additional 3 days and were provided with fresh media daily. 6-day cultures were inverted, placed on cover slips and live-imaged with a spinning disk confocal microscope in a temperature- and CO<sub>2</sub>-controlled incubation chamber.

#### **Proliferation and Cell Cycle Analysis**

Cells were plated as described for western blotting above and were incubated with appropriate drug/growth factor/optogenetic stimuli for 22 h before analysis. Cells were then trypsinized, spun down, and resuspended in PBS containing 0.1% Triton X-100, 200 μg/mL propidium iodide (Sigma), and 200 μg/mL RNAse A (Sigma) to lightly permeabilize and stain for DNA content. Samples were incubated in the dark for 20-30 min and analyzed by flow cytometry (Darzynkiewicz and Juan, 2001). 20,000 single cells were analyzed for each experimental replicate. All flow cytometry was performed on a BD LRSII Multi-Laser Analyzer using a 561-nm laser. Cell cycle fractions were determined using FlowJo V.X software by Watson (Pragmatic) modeling.

### **QUANTIFICATION AND STATISTICAL ANALYSIS**

Statistical significance was determined using a standard t-test for p-values. For Figure 4, p-values were calculated using a two-sided t-test assuming equal variances because we sought to test for both positive and negative effects on signaling dynamics by small molecules. For Figures 5 and 6, p-values were calculated using a one-sided t-test assuming equal variances because we specifically tested the hypothesis that each treatment would alter cell proliferation in proportion to its effect on Erk dynamics (e.g., increased Erk -> increased proliferation). Statistical tests and significance thresholds can be found in the figure legends for every figure containing a statistical comparison.

### **DATA AND CODE AVAILABILITY**

All Jython and MATLAB code is available on Github (github.com/toettchlab/Goglia2019). All time-lapse microscopy data from the small-molecule screen are available at the Image Data Resource (idr.openmicroscopy.org/; accession number idr0064).

# **Supplemental Information**

# A Live-Cell Screen for Altered Erk Dynamics

# **Reveals Principles of Proliferative Control**

Alexander G. Goglia, Maxwell Z. Wilson, Siddhartha G. Jena, Jillian Silbert, Lena P. Basta, Danelle Devenport, and Jared E. Toettcher

# Supplementary Materials for

# A live-cell screen for altered Erk dynamics reveals principles of proliferative control

Alexander G. Goglia<sup>1\*</sup>, Maxwell Z. Wilson<sup>1\*</sup>, Siddhartha G. Jena<sup>1</sup>, Jillian Silbert<sup>1</sup>, Lena P. Basta<sup>1</sup>, Danelle Devenport<sup>1</sup>, Jared E. Toettcher<sup>1</sup>

\* Equal contribution Correspondence to: toettcher@princeton.edu

### This PDF file includes:

Supplementary Figures 1-8 Supplementary Tables 1 and 2 Supplementary Video 1-5 Legends

## **Supplementary Figures and Legends**

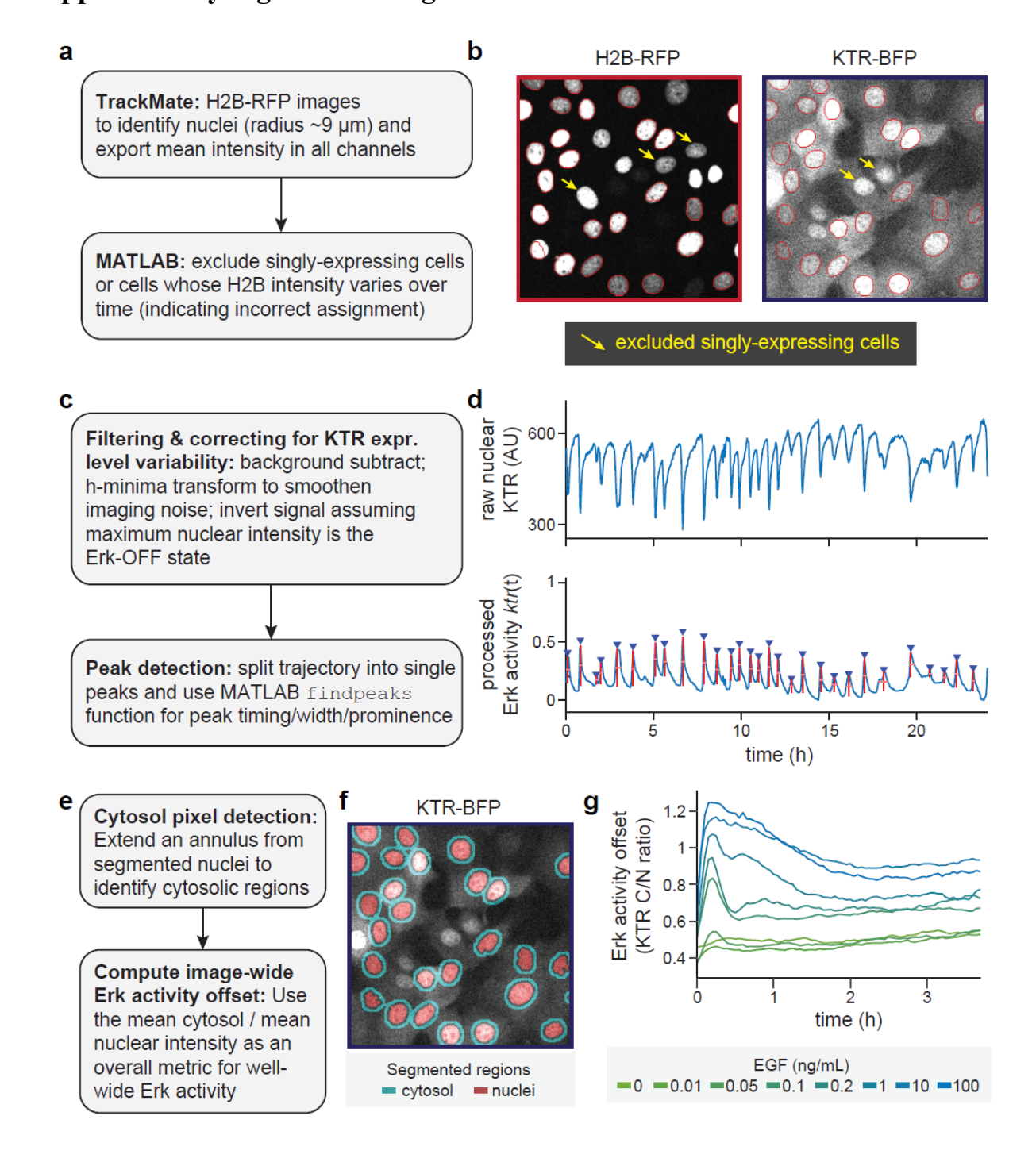


Figure S1, related to Figure 1. Data processing pipeline for microscopy data of Erk activity. (A,C,E) Schematics of each component of the data processing pipeline that takes in multichannel TIFF image stacks of H2B-RFP and KTR-BFP as inputs, and returns quantitative data about single-cell Erk dynamics. (B) Images of H2B and KTR images where nuclei have been automatically identified (red circles). Nuclei are excluded that only express one of the two components (yellow arrows). (D) Filtering and processing of Erk activity trajectories. Representative trajectory of nuclear KTR fluorescence from a single keratinocyte over time (upper panel) is h-minima transformed, inverted, and subjected to peak-finding (lower panel). Erk activity pulse timing (blue triangles), pulse prominence (red vertical bars), and pulse width (pink horizontal bars) are obtained for each trajectory. (F) For quantifying well-averaged Erk activity, cytosolic regions are computed by a combination of dilation and erosion operations to define regions outside of nuclei. The ratio of the mean cytosolic and nuclear pixel intensities is used as a quantitative metric of the overall Erk activity offset at each timepoint. (G) Quantifying Erk activity offset across populations of keratinocytes stimulated with EGF demonstrates that a pulsatile Erk response can be sensitively detected for EGF concentrations as low as 50 pg/mL.

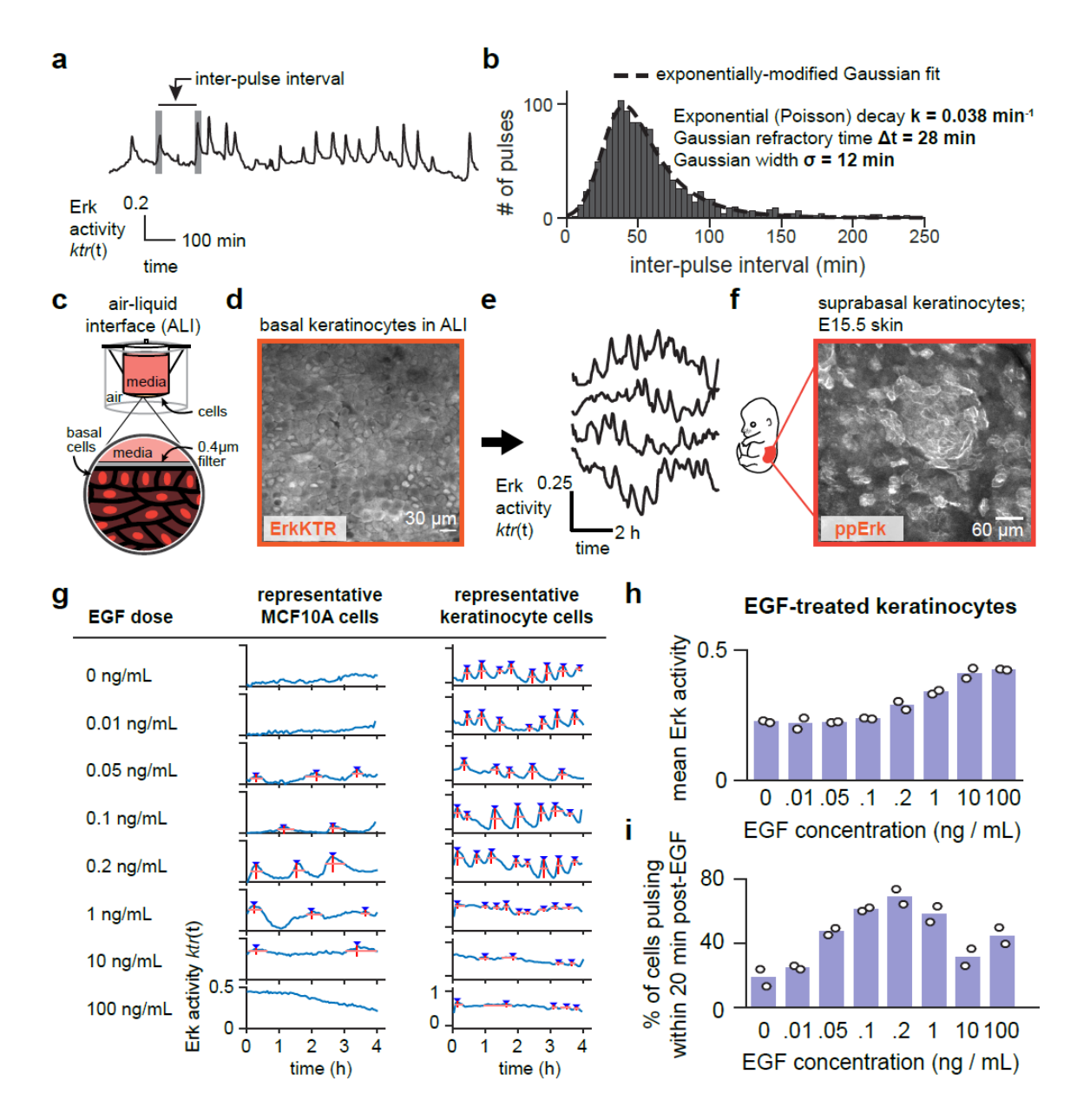
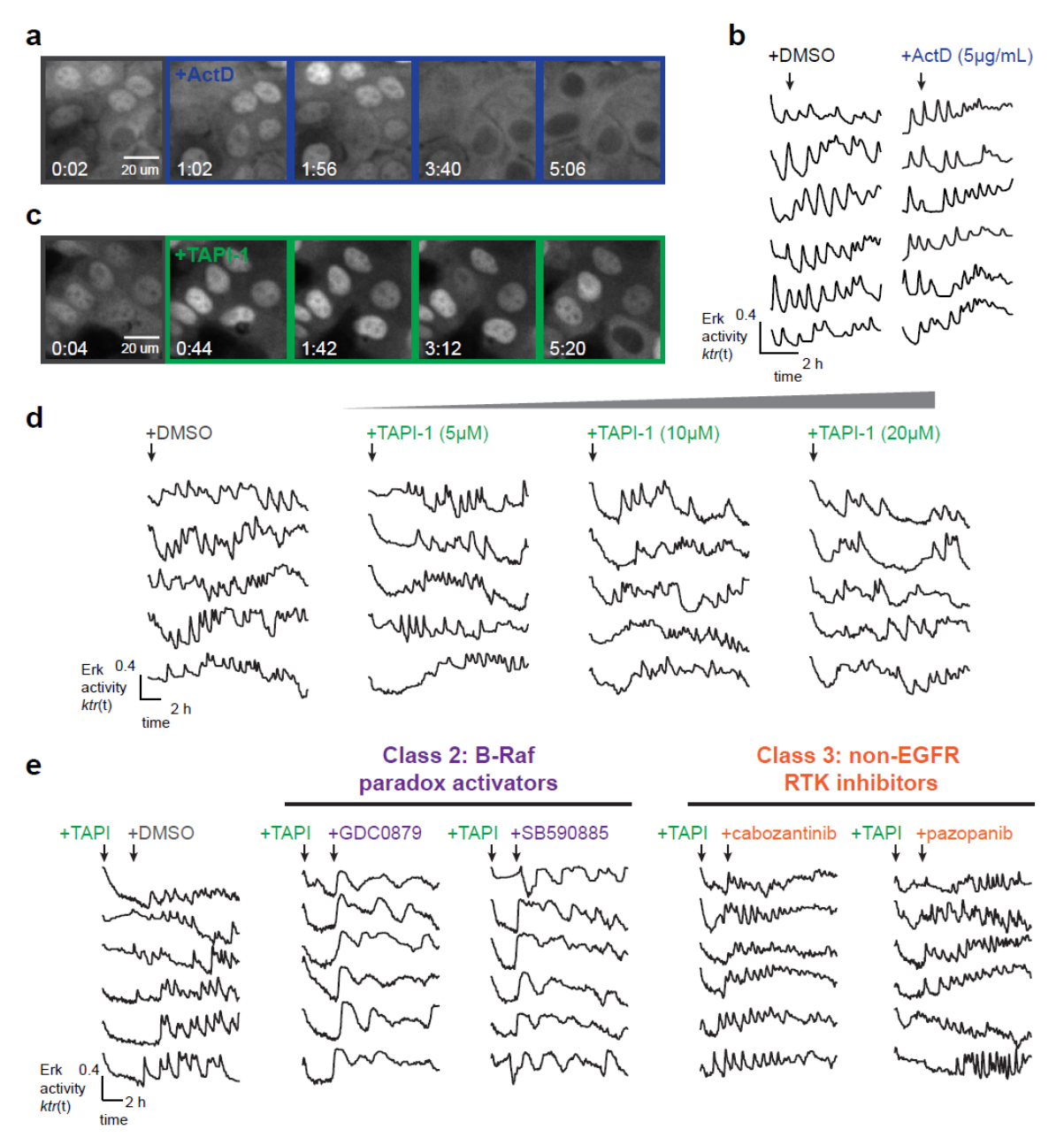


Figure S2, related to Figure 2. Comparing and quantifying Erk dynamics in keratinocytes and MCF10A cells. (A-B) Quantifying the distribution of 'inter-pulse intervals' (depicted in A) can be used to characterize the extent of periodic vs stochastic pulses. A tight Gaussian distribution at a single value is indicative of a periodic system; an exponentially-decaying tail indicates stochastic pulses firing at a characteristic rate. An admixture of periodic and stochastic behavior would generate a Gaussian-exponential distribution (in **B**). The distribution of intervals between each Erk pulse over a 24 h timecourse is depicted here (gray bars), fit to an exponentially-modified Gaussian distribution (dotted black line). Parameters of the fit indicate the exponential decay time and Gaussian time between periodic pulses. (C) Schematic of organotypic air-liquid interface (ALI) keratinocyte culture (see Methods). Cells are cultured on a hanging insert exposed to media on their basal surface. (D) Confocal image of the basal layer of KTR-H2B keratinocytes grown as an ALI for 6 d. (E) Representative Erk activity trajectories for cells in **D** imaged over time. (F) Images of whole-mount epidermis taken from E15.5 mouse embryos and immunostained for phospho-Erk1/2 (See Methods). (G) Representative Erk activity traces and identified pulses from single MCF10A (left) or primary keratinocyte (right) cells treated with increasing doses of EGF. (H-I) Average Erk activity offset a (in H) and the fraction of cells pulsing within 20 min of EGF treatment (in I) for keratinocytes treated with the indicated dose of EGF. A maximal pulsatile response is observed at 200 pg/mL of EGF, whereas maximum overall Erk activity is observed at 10 ng/mL. Each biological replicate (white circle) represents dynamics assessed from at least 100 single cells.



**Figure S3, related to Figure 2. Pulsatile Erk dynamics in keratinocytes persist in the absence of active transcription or ADAM-family protease activity.** (**A**) ErkKTR-BFP images of KTR-H2B keratinocytes treated with the transcription inhibitor actinomycin D (ActD; 5 μg/mL). Cells were incubated in GF-free media for 8 h and then imaged every 2 min over 6 h, with ActD added after 1 h of imaging. (**B**) Single-cell Erk activity traces from cells treated as in **A** with either DMSO (left) or ActD (right). (**C**) ErkKTR-BFP images from keratinocytes treated with 10 μM TAPI-1 an inhibitor of extracellular ADAM-family proteases. Cells were incubated in GF-free media for 8 h and then imaged every 2 min for 12 h, with drug added after 10 min of imaging. (**D**) Erk activity traces of keratinocytes treated as in **C** with either DMSO (left) or the TAPI-1 (right). (**E**) Erk activity traces of keratinocytes treated with 10 μM TAPI-1 (added after 10 min of imaging) and then either DMSO, a Class 2 compound, or a Class 3 compound (each added after 3 h of imaging). Cells were imaged every 2 min for 14 h.

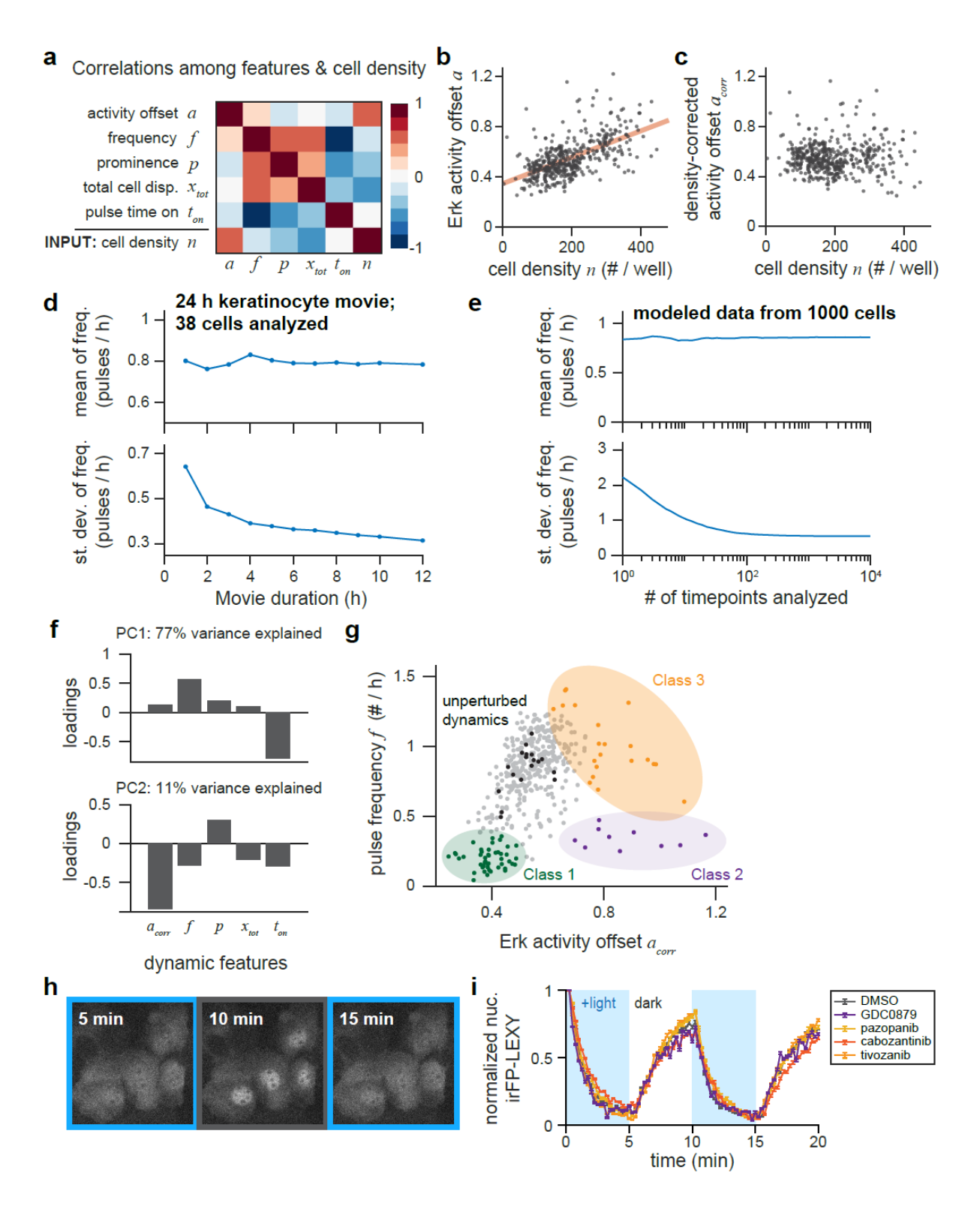


Figure S4, related to Figure 3. Additional analyses for the signaling dynamics drug screen. (A) Correlation coefficients between measurements computed across responses from all compounds in the small molecule screen. In addition to the four dynamic parameters  $(a, f, p, t_{on})$ , correlations were also measured for cells' total displacement  $(x_{tot})$  as well as one independent, experimentalist-controlled variable: cell density (n). The high correlation observed between cell density n and activity offset a suggested that a correction could separate drug-induced changes in Erk activity from those dependent on cell density, a drug-independent variable. (B) Plot of Erk activity a as a function of cell density n, with best-fit line shown in red. (C) Plot of densitycorrected Erk activity offset  $a_{corr}$  as a function of cell density n, computed by subtracting the expected offset value based on cell density (red line in **B**) from the measured offset and adding a constant value to ensure that  $\langle a_{corr} \rangle = \langle a \rangle$ . (**D**) The mean and standard deviation of single-cell frequencies f were extracted for the same 38 individual keratinocytes over different total observation windows, ranging from 1 h to 24 h, showing marked differences in convergence as a function of observation time. (E) Synthetic, modeled pulse data exhibits a similar trend, with rapid convergence of mean pulse frequency but slow convergence of estimates of cell-to-cell variability. (F) Plots of the contribution of each dynamic feature onto the first two principal components. PC1 is dominated by time-related parameters (frequency f and time on  $t_{on}$ ), whereas PC2 is dominated by amplitude-related parameters (Erk offset  $a_{corr}$  and pulse prominence p). (G) Plot of drug screen hits from all three classes on a plot of Erk activity offset  $a_{corr}$  versus pulse frequency f, demonstrating that all three classes of response can be separated by these two parameters. (H) Representative images of primary keratinocytes expressing infrared fluorescent protein (iRFP) -tagged LEXY, an optogenetic tool that enables blue light-induced nuclear export. Cells were imaged every 30 sec for 20 min while 450 nm blue light was toggled on (inducing nuclear export of iRFP-LEXY) and off (allowing nuclear recovery of unstimulated iRFP-LEXY). (I) Relative nuclear fluorescence of keratinocytes expressing iRFP-LEXY and imaged/stimulated as described in H. Cells were starved in GF-free media for 8 h and pre-treated with either DMSO vehicle control (gray), a Class 2 B-Raf inhibitor (purple), or a Class 3 RTK inhibitor (orange). Points (mean  $\pm$  SEM, n = 10 cells each) are normalized to the unstimulated initial value.

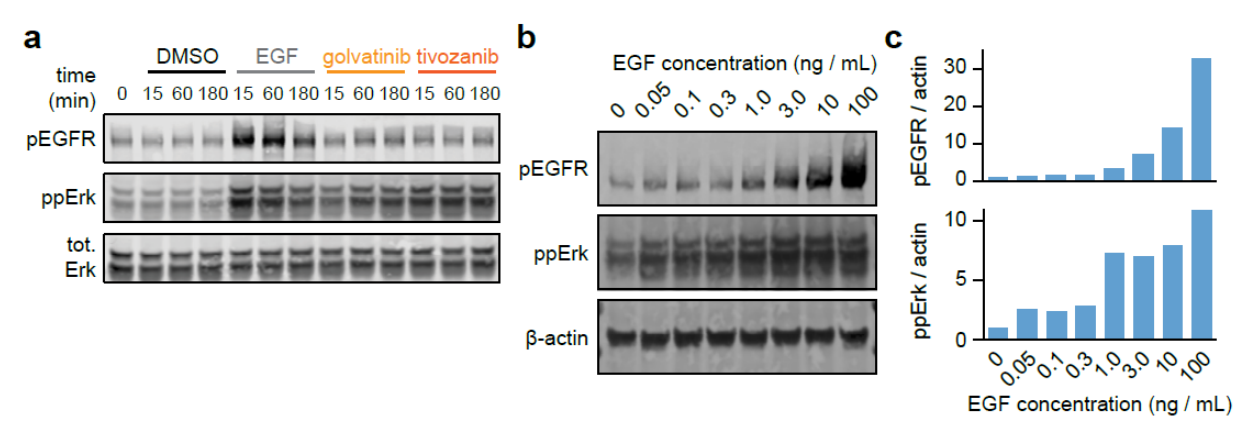


Figure S5, related to Figure 4. Erk and EGFR phosphorylation in response to Class 2/3 compounds and across doses of EGF. (A) A single gel was split and incubated with rabbit antiphospho-EGFR (pEGFR), rabbit anti-dually-phosphorylated Erk (ppErk), and mouse anti-total Erk antibodies as indicated. Lysates were collected at indicated timepoints after stimulation with EGF, golvatinib, tivozanib, or DMSO as a loading control. Quantification of the Western blot is presented in Figure 4D-E. (B) A single gel was split and probed with rabbit anti-phospho-EGFR (pEGFR), rabbit anti-dually-phospho-Erk (ppErk), and mouse anti-β-actin antibodies as indicated. Lysates were collected at 15 min after EGF addition. Keratinocytes were starved in GF-free media for 8 h prior to stimulation. (C) Quantification of pEGFR (upper panel) and ppErk (lower panel) from Western blot shown in B. pEGFR and ppErk levels are normalized to β-actin loading control and each value is represented as fold-induction relative to the untreated initial timepoint.

Figure S6, related to Figure 5. Drug-altered Erk dynamics from keratinocytes cultured in complete media. (A) Representative traces from keratinocytes grown in complete media that were treated with either a Class 2 B-Raf inhibitor, a Class 3 RTK inhibitor, or DMSO as a control. Cells were imaged every 3 min over 12 h. (B-C) Average Erk pulse frequencies (in B) and overall Erk activity offset (in C) for keratinocytes treated as in A. Each biological replicate (white circle) represents dynamics assessed from at least 100 single cells. Statistics are derived using a two-sided t-test (\*, p < 0.05; \*\*\*, p < 0.01; \*\*\*\*, p < 0.001).

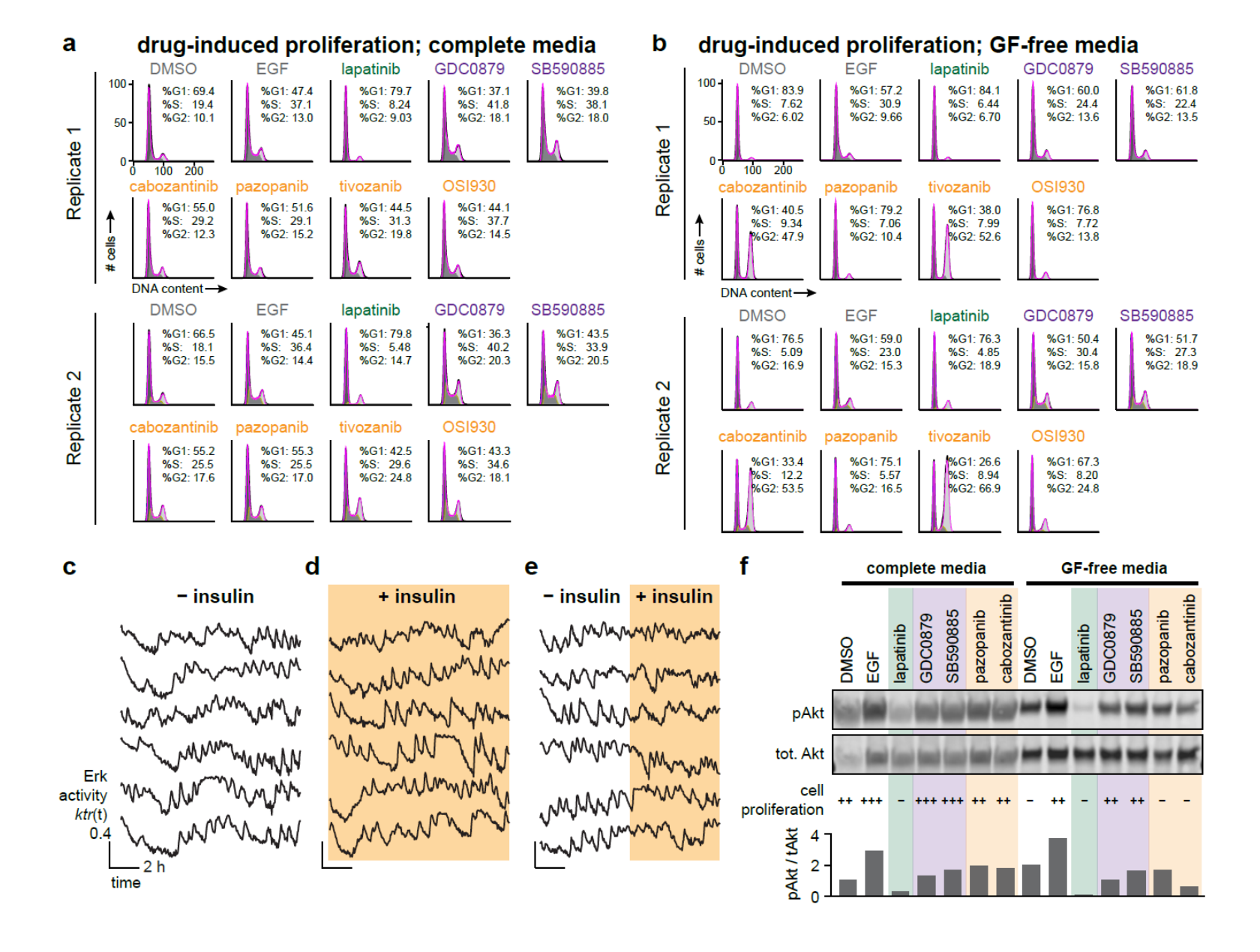
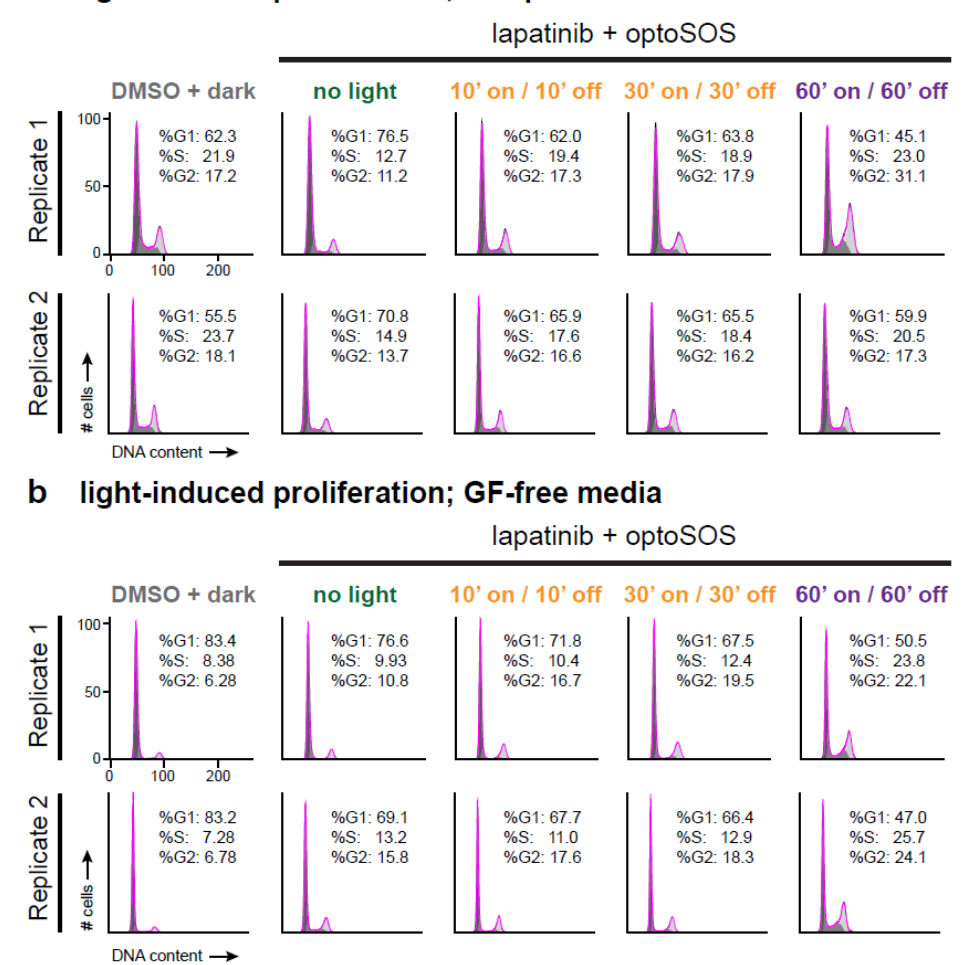


Figure S7, related to Figure 5. Cell proliferation in response to Erk dynamics-altering drugs. (A) DNA content distributions from keratinocytes grown in complete media for 22 h in the presence of selected Class 1, 2, or 3 kinase inhibitors. Two biological replicates are shown. with each stimulus condition containing data from at least 20,000 single cells. (B) DNA content distributions from keratinocytes grown in GF-free media for 22 h in the presence of selected Class 1, 2, or 3 kinase inhibitors. Two biological replicates are shown, with each stimulus condition containing data from at least 20,000 single cells. (C-E) Representative ErkKTR-BFP images from a timecourse of KTR-H2B keratinocytes imaged with (**D**) and without (**C**) insulin. Cells were first incubated for 8 h in either GF-free media or GF-free media supplemented with 5 μg/mL insulin. Cells were then imaged every 2 min for 10 h, with insulin added to the indicated cells (E) to a final concentration of 5 µg/mL after 5 h of imaging. (F) Top panel: Western blot for Akt phosphorylation after treatment with Class 1, 2, or 3 compounds in either complete or GF-free media. Lysates were collected after 1 h of stimulation with EGF, a Class 2 paradoxactivating BRaf inhibitor (purple), a Class 3 non-EGFR RTK inhibitor (orange), or DMSO as a vehicle control in either complete media (left) or GF-free media (right). Middle panel: the extent of cell proliferation under the same condition from Figure 5C-D is indicated by symbols ("-" for 0-10% of cells in S-phase; "+" for 10-20%; "++" for 20-30%; "+++" for 30-40%). Bottom panel: quantification of phospho-Akt levels normalized to total-Akt for each condition.

### a light-induced proliferation; complete media



**Figure S8, related to Figure 6. Cell proliferation in response to dynamic optogenetic Ras/Erk stimuli.** (**A**) DNA content distributions from OptoSOS keratinocytes grown in complete media for 22 h and stimulated with light inputs mimicking the Erk dynamics induced by Class 1, 2, or 3 kinase inhibitors. Two biological replicates are shown, with each stimulus condition containing data from at least 20,000 single cells. (**B**) DNA content distributions from OptoSOS keratinocytes grown in GF-free media for 22 h and stimulated with light inputs mimicking the Erk dynamics induced by Class 1, 2, or 3 kinase inhibitors. Two biological replicates are shown, with each stimulus condition containing data from at least 20,000 single cells.

## **Supplementary Tables**

Table S1, Related to STAR Methods: Class 1, 2, and 3 drugs and their validated targets. Targets were obtained from the LINCS database (Keenan et al., 2018; Moret et al., 2019) and from Selleck Chemicals' annotation of their kinase inhibitor compound library. Similar isoforms were condensed into a single target class (e.g., MEK1 and MEK2: MEK; AurKA, AurKB, AurKC: AurK). From the Validated Targets list, targets within each class that function as EGFR/MEK/ERK inhibitors were annotated green, paradox-activating B-Raf inhibitors were annotated purple, and non-ErbB RTK inhibitors were annotated yellow.

	Product Name	Validated Targets	EGFR / MEK / ERK	RAF	Non- ErbB RTK
	Selumetinib (AZD6244)	MEK			
	Afatinib (BIBW2992)	ABL, BLK, DYRK EPHA, ERBB, GAK, HIPK, IRAK, LCK			
	Dasatinib	ABL, BLK, BTK, CSF1R, DDR, EPHA, EPHB, ERBB, FGR, FRK, FYN, GAK, JAK, KIT, LCK, LYN, MAP3K19, MAP4K5, MINK1, MKK5, PDGFR, RAF, RET, RIPK, SLK, SRC, TKT, TNK, TYK2, YES1			
CLASS	Gefitinib (ZD1839)	ABL, CDK, CSNK, EPHA, ERBB, GAK, HIPK, IRAK, LCK, LYN, MAP3K19, MKK5, MKNK, RIPK, SLK, STK10			
1	Lapatinib (GW-572016) Ditosylate	ERBB, RAF			
	PD0325901	MEK			
	AC480 (BMS-599626)	ERBB			
	SL-327	MEK			
	Refametinib (RDEA119, Bay 86-9766)	MEK			
	WZ3146	ERBB			
	WZ8040	ERBB			
	CUDC-101	ERBB			
	Pelitinib (EKB-569)	ABL, AXL, BLK, CSNK, ERBB, FGR, FRK, GAK, JAK, LCK, LYN, MAP4K5, MEK, SLK, SRC, STK10, YES1			
	Pimasertib (AS-703026)	MEK			
	AEE788	ERBB, VEGFR			

(NVP-AEE788)	
AZD7762	ABL, ALK, AXL, BLK, CSF1R, DDR, DYRK, EPHA, ERBB, FLT3, FYN, IRAK, JAK, KIT, LCK, MAP3K19, MEK, MKK5, MKNK, NUAK, PDGFR, PKC, PKN, PLK, PTK2, RET, SLK, SRC, STK10, TRK, VEGFR
PD318088	MEK
Sapitinib (AZD8931)	ERBB
OSI-420	ERBB
TAK-733	MEK
Trametinib (GSK1120212)	MEK
Ibrutinib (PCI-32765)	AURK, BLK, BTK, EPHB, ERBB, FGFR, JAK, LCK, MKK5, NUAK, PKD, RET, RIPK, SRC, TIE, TRK, VEGFR, YES1
Tyrphostin AG-1478	ABL, ERBB, GAK, MKNK
TAK-285	ERBB
WHI-P154	ERBB, JAK
Icotinib	ERBB
Binimetinib (MEK162, ARRY-162, ARRY-438162)	MEK
Osimertinib (AZD9291)	ERBB
Ulixertinib (BVD-523, VRT752271)	ERK
AZD3759	ERBB
Cobimetinib (GDC-0973, RG7420)	MEK
Olmutinib (HM61713, BI 1482694)	ERBB
Saracatinib (AZD0530)	ABL, KIT, LCK, SRC, YES1
SP600125	JNK, MKNK
Hesperadin	AURK
TWS119	GSK3

	AZ 960	JAK	
	Volasertib (BI 6727)	PLK	
	Omipalisib (GSK2126458, GSK458)	MTOR, PIK3C	
	WYE-125132 (WYE-132)	MTOR	
	NVP-BSK805 2HCl	JAK	
	ZM 306416	VEGFR	
	Ro3280	PLK	
	GDC-0879	CSNK, MAP3K19, RAF	
	SB590885	RAF	
	Dovitinib (TKI-258, CHIR- 258)	ABL, AMPK, AURK, BLK, CDK, CSF1R, CSNK, EPHB, FGFR, FGR, FLT3, FYN, GAK, GSK3, HIPK, IKBK, IRAK, JAK, KIT, LCK, LYN, MAP3K19, MAP4K5, MEK, MINK1, MKK5, MYLK, NUAK, PDGFR, PKN, PLK, RET, RIPK, ROCK, RPS6KA, SLK, STK10, TRK, VEGFR, YES1	
CLASS 2	Dovitinib (TKI-258) Dilactic Acid	ABL, AMPK, AURK, BLK, CDK, CSF1R, CSNK, EPHB, FGFR, FGR, FLT3, FYN, GAK, GSK3, HIPK, IKBK, IRAK, JAK, KIT, LCK, LYN, MAP3K19, MAP4K5, MEK, MINK1, MKK5, MYLK, NUAK, PDGFR, PKN, PLK, RET, RIPK, ROCK, RPS6KA, SLK, STK10, TRK, VEGFR, YES1	
	Rebastinib	ABL, FGR, FLT3, LYN, SRC, TIE,	
	(DCC-2036)	VEGFR, YES1	
	A-674563	AKT, CDK MTOR	
	AZD8055 LY2090314	AMPK, CDK, CLK, GSK3, LCK, PKC, PKN	
	abemaciclib (LY2835219)	CDK	
	SC1	ERK	
	SGI-7079	VEGFR	
	Pazopanib HCI (GW786034 HCI)	ABL, AURK, CSF1R, DDR, EPHB, FGFR, FRK, IRAK, KIT, LYN, MAP3K19, MKK5, PDGFR, PLK, RAF, RET, RIPK, SLK, STK10, TIE, VEGFR	

AURK, ERBB, FYN, LCK, MEK, ZM 447439 PDGFR, RET, ROCK, VEGFR Danusertib ABL, AURK, FGFR, RET (PHA-739358) ABL, AMPK, AURK, BLK, CDK, CLK, CSF1R, DDR, EPHA, EPHB, ERBB, FGFR, FLT3, FRK, FYN, HIPK, IRAK, Foretinib JNK, KIT, LCK, LYN, MAP3K19, (GSK1363089) **CLASS** MEK, MET, MKK5, PDGFR, PLK, RET, RIPK, SLK, SRC, STK10, TIE, TRK, VEGFR, YES1 MET JNJ-38877605 Cabozantinib FLT3, KIT, MET, RET, TIE, TRK, (XL184, **VEGFR** BMS-907351) BMS-754807 MET, TRK ABL, AURK, FGFR, FLT3, GSK3, AT9283 JAK, RET, S6K, VEGFR, YES1 AURK, EPHB, ERBB, FLT3, HIPK, Barasertib (AZD1152-KIT, LCK, MKK5, PDGFR, RET, TIE, HQPA) **VEGFR** CDK, EPHB, MEK, MKK5, PDGFR, PLX-4720 RAF, RIPK **CYC116** AURK, VEGFR FGFR, KIT, PDGFR, RAF, RET, TIE, Regorafenib (BAY 73-4506) **VEGFR** CHIR-99021 ABL, FYN, GSK3, VEGFR (CT99021) PD173074 FGFR, VEGFR Golvatinib MET, VEGFR (E7050) 7.8-**TRK** Dihydroxyflavone LY294002 CSNK, GSK3, MTOR, PIK3C OSU-03012 (AR-**PDK** 12) SNS-032 CDK, CLK, CSNK, GSK3 (BMS-387032) PD98059 MEK AT7867 S6K Uprosertib **AKT** (GSK2141795) AT13148 ROCK, S6K Butein **ERBB MTOR** ETP-46464

Table S2, Related to STAR Methods: Media recipes used for keratinocyte culture.

